skb.se

SKB P-22-22

ISSN 1651-4416
ID 1981459
November 2022

Modelleing buffer upwards expansion

Ola Kristensson
Clay Technology

Keywords: Buffer, Swelling, Bentonite, Simulation, Friction

This report concerns a study which was conducted for Svensk Kärnbränslehantering AB (SKB). The conclusions and viewpoints presented in the report are those of the author. SKB may draw modified conclusions, based on additional literature sources and/or expert opinions.

Data in SKB's database can be changed for different reasons. Minor changes in SKB's database will not necessarily result in a revised report. Data revisions may also be presented as supplements, available at www.skb.se.

This report is published on www.skb.se

Abstract

Hydraulic and mechanical behaviour of a deposition hole buffer in a simplified isothermal KBS-3V setup is here investigated numerically. An extreme scenario is considered, the tunnel backfill remains dry during water uptake of the deposition hole buffer. This is studied when allowing for friction along the deposition hole wall. Several variants are simulated, analysed, and compared. Buffer heave, reaction pressure at the buffer/tunnel backfill interface, and dry density fields are reported for all cases.

Sammanfattning

Här redovisas en numerisk undersökning av hur bufferten i en förenklad isoterm uppställning baserad på KBS-3V beter sig hydrauliskt och mekaniskt. Det undersökta scenariot är extremt, tunnelåterfyllnaden antas vara torr under det att bufferten i deponeringshålet tar upp vatten. Modellerna tar hänsyn till friktion mellan bufferten och deponeringshålsväggen. Olika varianter simuleras, analyseras och jämförs. Buffertuppsvällning, reaktionskraften vid gränssnittet mellan buffert och tunnelåterfyllning och torrdensitetsfält rapporteras för alla fallen.

Table of Contents

1 Introduction 3

2 Model description 5
2.1 Geometry and constituents 5
2.2 Initial and boundary conditions 6
2.3 Material representations 8
2.3.1 Porous media 8
2.3.2 Solid phase 9
2.3.3 Liquid phase 10
2.3.4 Gas phase 11

3 Comments regarding the model setup 12
3.1 Swelling pressure curves 12
3.2 Calibrating BBM for the buffer materials 12
3.3 Hydraulic representation of buffer materials 15
3.3.1 Retention 15
3.3.2 Initial setting of the porosity dependent permeability 15
3.3.3 Diffusivity analysis, updated porosity dependent permeability 16
3.4 Mechanical representation of the TB 17

4 Results from the first set of simulations 19
4.1 Evaluation of the Base Case simulation 19
4.2 Requested results from the first set of simulations 22

5 Results from the second set of simulations 26
5.1 Mesh dependency study 26
5.2 Requested results from the second set of simulations 27

6 Discussion and analysis 30
6.1 Pressure criterion vs. dry density criterion 30
6.2 First set of cases 32
6.3 Second set of cases 36

7 Conclusions 40

References 41

Appendix A Theory 42

Appendix B Model identification 46

1 Introduction

In this work the hydraulic-mechanical behaviour of a buffer in a simplified isothermal KBS-3V setup is investigated. An extreme scenario is considered, the tunnel backfill maintains dry while the buffer in the deposition hole takes up water. This could lead to significant buffer upwards expansion and therefore low pressures in the buffer. Since low pressures promote microbial activity in the buffer and thereby sulphide driven copper corrosion (see Posiva SKB 2017), there is an interest in investigating this scenario.

One reason for carrying out new simulations of this kind is to study how incorporation of wall friction between the buffer and deposition hole wall affect the solution. In existing analyses, friction-free conditions have often been assumed at this interface and this could give overly conservative assessments.

A first set of simulations, {Base Case, Case 1, … , Case 5}, consisting of cases with alternative: tunnel backfill retainment (generating the axial pressure), initial buffer block dry density, and water inflow scenarios, are studied with a rock wall friction specified to have a friction angle of 7.2°. Definitions of the cases within the first set are given in Table 1-1. In the following, Base Case is abbreviated BC and Case *N* by C*N*.

Table 1-1. First set of cases.

	Base case	Case 1	Case 2	Case 3	Case 4	Case 5	Case 6
Axial pressure	Spring load k=20 MPa/m	Constant 1.5 MPa	Spring load k=750 kPa/m	Spring load k=20 MPa/m	Spring load k=20 MPa/m	Spring load k=20 MPa/m	Spring load k=20 MPa/m
Wetting	Side boundary	Side boundary	Side boundary	Bottom boundary	Side boundary	Side boundary	Bottom boundary
Block dry density	1613 kg/m^3	1613 kg/m^3	1613 kg/m^3	1613 kg/m^3	1479 kg/m^3	1670 kg/m^3	1613 kg/m^3
Water content	17 %	17 %	17 %	17 %	17 %	17 %	saturated

A second set of four additionally requested cases, was dealt with at a later stage. The additional cases address two alternative rock wall friction angles, 5° and 1°, with setups otherwise identical to the setups of updated/improved versions of the BC and C2, see Table 1-2. The second set of simulations also contains the updated BC and C2 realisations, using the original friction angle of 7.2°, as well as realisations where roller boundary conditions are prescribed at the interface between the deposition hole wall and buffer material. Thus, the second set of simulations is {BC:7.2°, BC:5°, BC:1°, BC:rollers, C2:7.2°, C2:5°, C2:1°, C2:rollers}.

Table 1-2. Second set of cases.

	Base Case: 5°	Base Case: 1°	Case 2: 5°	Case 2: 1°
Friction angle	5°	1°	5°	1°

The models simulate hydraulic and mechanical processes and are solved using the finite element solver Code_Bright, developed for analysing porous geotechnical systems. The theoretical basis of the formulation is described in Appendix A. The results in this report were generated using Code_Bright v2020_21 and v2021_22.

Much of the effort in this work is to investigate the effect from incorporating friction between the buffer and its surroundings. It is therefore of importance to understand and represent the friction correctly. There are several interfaces where friction may occur within and at the boundary of the buffer. Friction may take place at the interfaces between block (B) and the pellet-filled slot (PS) and the PS and the rock wall. Friction may also take place within the PS itself.

To simplify the reasoning the evolution of the system is divided in three phases: initial, intermediate, and final. The initial phase is characterised by unsaturation, low pressure, and low density. The characteristics of the final phase are saturation, significant pressure and higher density.

Experimental investigations of PS under conditions similar to those of the initial phase can be found in Appendix F in Glamheden et al. (2010). The determined internal friction angle was 36°, the interface between B and PS had a friction angle of 21°, and the interface between the PS and rock wall a friction angle of 33°.

If assuming significant homogenisation, i.e. B-like properties for the PS material, and a strong bond between B and PS, the final state description can be considered being specified by the friction at the PS-rock interface only. Experiments determining the properties at a B-rock interface can be found in Dueck et al. (2019), see Figure 1-1. In Dueck et al. (2019) it was concluded that the friction angle at the interface was about half the internal friction angle. With a swelling pressure somewhere between 1 and 6 MPa the data indicates an interface friction angle somewhere between 4.5°-7.5°. Figure 1-1 also indicates that there is a peak and residual value of the friction angle.

The behaviour in the intermediate phase is unknown. A pragmatic approach, given the lack of direct information, would be to assume that one may interpolate between what is known for the initial and final phase.

If taking the pragmatic approach and considering the information and assumptions made above correct, use of constant friction properties, equal to what is found for the final phase, should be appropriate for obtaining conservative assessments regarding a lower pressure limit linked to deactivation of microbial activity. Thus, using a representation where the friction between B and rock wall is described using a friction angle about 7.2° seems appropriate.

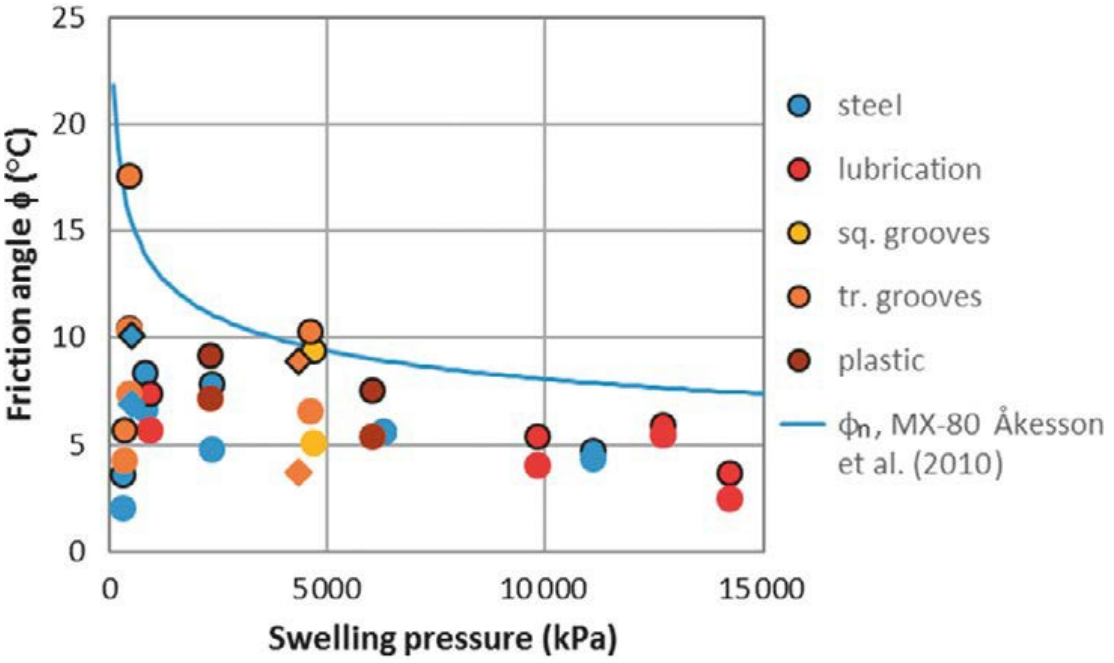

Figure 1-1. From Dueck et al.(2019, Figure 3-9). Friction angle as a function of swelling pressure from tests on MX-80 (circles) and Calcigel (diamonds) in the series with friction tests. The swelling pressure was measured radially. Marker lines around the symbols represent peak values and no marker lines represent residual values.

The report begins with a specification of the models' setup in chapter 2, which is complemented by more details given in chapter 3. Thereafter follows the results of the simulations in the first set of cases in chapter 4 and the second set of cases in chapter 5. Chapter 6 contain discussion and analysis and finally in chapter 7 conclusions are given. More information about the theory of Code_Bright is found in Appendix A and Appendix B contains a list identifying the models.

2 Model description

The poromechanical formulation on which Code_Bright is based is described in Appendix A, for a more complete description see Alcoverro and Alonso (2001). Hydraulic and mechanical processes are here considered in the mixed initial/boundary value problem and the information required to fully define the problem is given below.

The buffer has a full two-way hydromechanical coupling whereas the tunnel backfill uses the option to uncouple volumetric deformation effects on hydraulics. The option of updated coordinates, resulting in a "partial updated Lagrangean formulation", has been used to bring the model one step closer to a large strain formulation. When using this option, the porosity field agrees with the obtained deformation field.

Below follows a description of the simulation setups used in the first set of cases, first geometry and ingoing constituents are described and thereafter follows the initial and boundary conditions. Last, constitutive relations are given together with parameter values. The changes made when addressing the second set of cases are described in chapter 5 where the results for the second set are given. Further details about the setup are given in chapter 3.

2.1 Geometry and constituents

In Figure 2-2, the geometry and constituents, present in one of the axisymmetric representations, are shown. An example of a discretization (mesh) is also indicated. The constituents are: Blocks (B), a Pellet-filled Slot (PS) and the Tunnel Backfill (TB) at the top. The close-up of the discretization shows the part where B, PS, and TB meet. Due to abrupt differences in material properties and boundary conditions at this location the solver has difficulties if no measures are taken. Different conditions were therefore sometimes used at this location to make simulations converge. The 3×3 cross-triangles shown in the close-up has a side length of 5 cm, so the "the 5 cm top part of the PS boundary", often addressed below, is the vertical outer boundary of the cross-triangles.

The assignment description specified the mechanical reaction of the TB in terms of a "spring stiffness". To obtain convergence of the simulations, different TB representations were used for different cases. The differences were: geometrical, material parameter values, and boundary condition specifications. Below, the different geometry and material configurations used is listed together with the models in which they were used, see also Figure 2-1 (the boundary conditions used in the different cases are given in the following section):

- In most of the cases (BC, C3, C4, and C5) the TB was represented by using a 10 m high cylinder containing two TB-materials with different stiffnesses. A softer pipe-shaped volume on top of the PS constituent surrounded a stiffer cylinder-shaped volume on top of the B constituent.
- For C1, a 1 m high cylinder, here also consisting of two TB-materials of different stiffnesses (a softer surrounding a stiffer), was given a 5 cm layer of the stiffer TB material on top.
- In C2 the TB constituent was represented by a 1 m high cylinder containing one material.

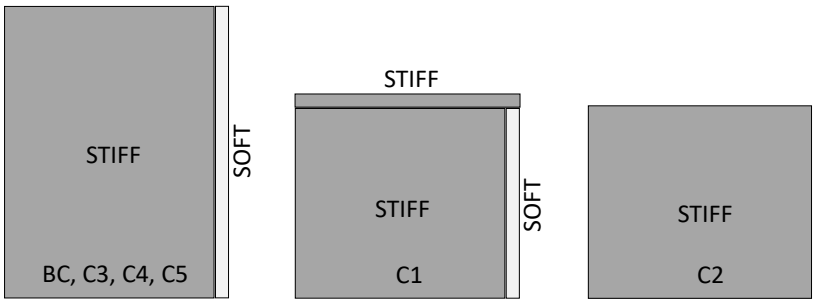

Figure 2-1. Schematic geometry (not to scale) and material arrangements of TB representations in different cases.

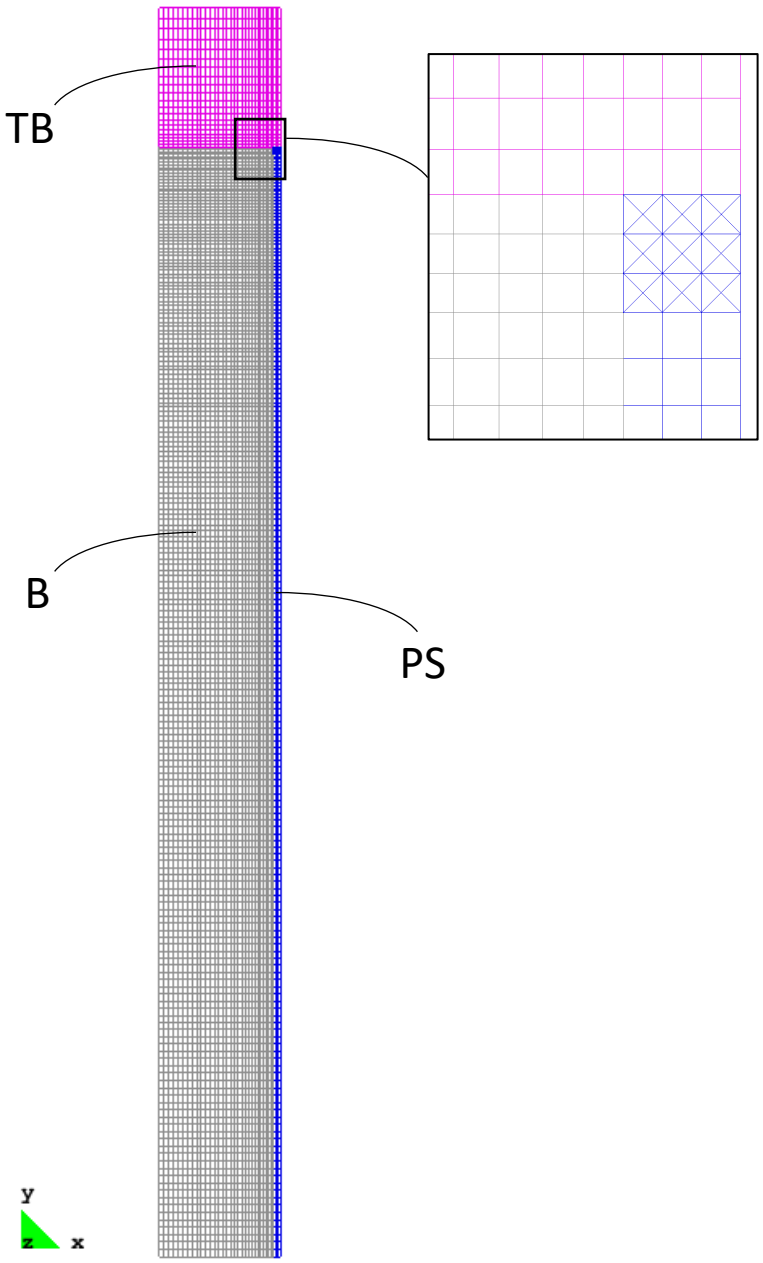

Constituents	
Name	**Description**
TB	Tunnel Backfill
B	Blocks
PS	Pellet-filled Slot

Discretization	
Name	**No. elem**
TB	Differs
B	30 × 203 ql
PS	3 × 200 ql 3 × 3 x-tri

Figure 2-2. Example of geometry, constituents, and discretization. The lower table describes the discretization where ql indicates quadrilaterals and x-tri cross-triangles which can be seen in the close-up. The 3 × 3 cross-triangles has a side length of 5 cm. Different cases had different TB representations, where most used several materials, i.e., the part indicated with TB in the geometry above is just one of many representations.

2.2 Initial and boundary conditions

In Code_Bright the initial conditions are given in terms of liquid pore pressure, p_l, stresses, $\boldsymbol{\sigma}$, and porosity, ϕ (which also can be expressed in terms of dry density, ρ_d). The initial conditions are specified in Table 2-1. The dry density of the TB is not presented since it is unimportant for this task. In the row indicated by B+PS the homogenized dry density and porosity are given.

Table 2-1. Initial conditions

Constituent	p_l [MPa]	σ_{ij}, $i = j$ [MPa]	ρ_d [kg/m^3]/ϕ [-]		
			BC	C4	C5
TB	-47.174	-0.101	*/0.9	*/0.9	*/0.9
B	-47.174	-0.101	1613/0.42	1479/0.47	1670/0.40
PS	-47.174	-0.101	950/0.66	950/0.66	950/0.66
B+PS			1540/0.45	1420/0.49	1590/0.43

The hydraulic boundary conditions were defined as follows. No flow conditions were applied on all boundaries except the inflow boundary. The hydraulic boundary conditions applied along the inflow boundary are given in Table 2-2. When inflow through the vertical boundary along the PS-material was considered, no flow conditions were applied on the 5 cm top part of the boundary.

Table 2-2. Hydraulic boundary conditions at the vertical PS boundary.

Time interval [days]	Condition [MPa]	Comment
$t^0 < t < t^0 + 1$	$p_l = p_l - ({p_l}^0 + 0.1)(t - t^0)$	Linear ramping from the initial unsaturated state to full access to water at atmospheric conditions.
$t > t^0 + 1$	$p_l = 0.1$	Full access to water at atmospheric conditions.

The mechanical boundary conditions were defined according to the following. Roller boundary conditions (no displacements in the normal direction and no change in traction in the tangential direction) were, for all cases, prescribed on the bottom boundary and all vertical boundaries other than that along the vertical PS boundary. For C1, roller conditions were also applied along the vertical PS boundary during the initial ramping of the vertical load.

Fixed boundary conditions were generally prescribed along the vertical PS boundary (except for C1 as described above). At the top 5 cm of the PS boundary however, the fixed condition was not prescribed as "strict" as in the boundary below it. It was given a lower "multiplier" in the boundary condition to: improve the convergency, decrease the disturbance from the material interfaces, and decrease the effect from the abrupt shift in type of boundary conditions (fixed/roller) at the PS/TB interface. To prescribe a fixed boundary condition, a multiplier of 1e10 MPa/m was generally used. The decreased multipliers used in the simulations are given in Table 2-3.

Table 2-3. Multipliers with unit [MPa/m] used in the mechanical boundary condition at the top 5 cm of vertical PS boundary.

BC	C1	C2	C3	C4	C5
1e6	1e8	1e7	1e6	1e6	1e6

The mechanical top boundary conditions of the TB representation differed between the cases. For the Base Case and C3 - C5, roller boundary conditions were used. For C1, no changes in traction were allowed in the tangential direction, and the load in the normal direction was ramped from the initial condition (-0.101 MPa) to -1.5 MPa during one day, whereafter it was held constant. Also, during the ramping, the stiffnesses of the buffer materials were set high to avoid large compressive deformations. For C2, no changes in traction were allowed in the tangential direction, and a "spring boundary condition" was used in the normal direction. The spring boundary condition was given by prescribing the initial load (-0.101 MPa) and specifying a spring constant (1.5 MPa/m). It should be noted that this spring constant were used together with a TB material stiffness to obtain a suitable combined stiffness.

2.3 Material representations

Constitutive relations and parameter values are given in this section. A brief description of how the parameter sets were obtained is given in the listing below. More information and references are given in chapter 3.

Hydraulic properties

- *TB*: "Inert" (should not affect the result)
- *B & PS*: Retention according to laboratory data
- *B & PS*: Permeability dependence on dry density according to laboratory data
- *B & PS*: Intrinsic & relative permeability from moisture diffusivity comparisons

Mechanical properties

- *TB*: According to what is given in the task description
- *B & PS*: The starting point was the setting used in Sandén et al. (2020), parameter setting in line with Åkesson et al. (2010), testing and calibration using 1D-simulations of B & PS working together.

2.3.1 Porous media

The retention is given by Classical van Genuchten,

$$\widetilde{S_l}(p_l) = \left(1 + \left(\frac{p_g - p_l}{P_0}\right)^{\frac{1}{1-\lambda}}\right)^{-\lambda}, \tag{2-1}$$

Values for parameters P_0 [MPa] and λ [-] are given in Table 2-4.

Table 2-4. Retention parameters of porous media.

Constituent	P_0 [MPa]	λ [-]
TB	0.171	0.2
B	BC: 7.366 C4: 2.864 C5: 11.427	BC: 0.18 C4: 0.18 C5: 0.18
PS	0.171	0.2

The advective mass flux, is given by Darcy's law:

$$\begin{gathered} \boldsymbol{q}_l = -\frac{\boldsymbol{k} k_{rl}}{\mu_l}(\nabla p_l - \rho_l \boldsymbol{g}) \\ \boldsymbol{k} = k_{in}\boldsymbol{I} \\ k_{rl} = {S_l}^n \end{gathered} \tag{2-2}$$

The intrinsic permeabilities and exponents for the relative permeability are given in Table 2-5.

Table 2-5. Intrinsic permeabilities and exponent in the law for the relative permeability of porous media.

Constituent	k_{in} [m²]	n [-]
TB	$2.4 \cdot 10^{-30}$	1
B	$1.8 \cdot 10^{-20}\exp(21.764(\phi - 0.5))$	5
PS	$2.4 \cdot 10^{-20}\exp(21.764(\phi - 0.5))$	1

2.3.2 Solid phase

The **solid phase density** is given by a constant,

$$\rho_s = \rho_{s0}\,, \tag{2-3}$$

and for the present models all materials are given the same value (see Table 2-6).

Table 2-6. Solid phase density.

Constituent	ρ_{s0} [kg/m^3]
TB	2780
B	2780
PS	2780

Table 2-7 shows an overview of the **mechanical material models** used for the solid phase in all materials. In the following tables, Table 2-8 and Table 2-9, the different mechanical material models are described, and the parameter values are given.

Table 2-7. Overview of the solid phase mechanical material models.

Constituent	Model	Comment
TB	Linear elastic	In BC, C1, C3, C4 and C5 two TB-materials were used, a stiffer on top of the B-constituent and a softer on top of the PS-constituent. In C2 a single TB-material was used where the stiffness was calibrated as to match the stiffness used in the "spring boundary condition".
B	Modified BBM	The parameter set used in Sandén et al. (2020) was the starting point. The new setups, for BC (C1, C2, C3), C4 and C5, was obtained by using what was given in Åkesson et al. (2010) as guidelines. Changes from the parameter set used in Sandén et al. (2020) were use of a constant critical state line parameter *M* and a constant tensile strength parameter p_s.
PS	Modified BBM	The parameter set used in Sandén et al. (2020) together with the given friction angle of 7.2 ° was the basis. The new setups for BC, C4 and C5, was obtained by using what was given in Åkesson et al. (2010) as guidelines. The setup was tested and calibrated using axisymmetric 1D models of the B-PS system and comparing the mechanical response with "typical" swelling pressure curves and void ratio profiles. p_{ref} was set lower as compared to Sandén et al. (2020).

Table 2-8. Linear elastic model and parameter values. The same values were used in BC, C1, C3, C4 and C5.

Total strain increment	$d\boldsymbol{\varepsilon} = d\boldsymbol{\varepsilon}^e$	**Parameter**	**TB**	**TB$_{soft}$**
Elastic strain increment:	$d\boldsymbol{\varepsilon}^e = -\frac{1}{3}d\varepsilon_v^e\mathbf{1} + d\boldsymbol{e}^e$ $d\varepsilon_v^e = \frac{dp'}{K}, K = \frac{E}{3(1-2\upsilon)}$ $d\boldsymbol{e}^e = \frac{d\boldsymbol{s}}{2G}, 2G = \frac{E}{1+\upsilon}$	***E* [MPa]**	BC: 200 C2: 1.5	BC: 2 C2: -
		v	0.0001	0.0001

Table 2-9. Modified BBM model and parameter values. The same values were used in BC, C1, C2, and C3.

		Parameter	B BC C4 C5	PS BC C4 C5
Total strain increment	$d\boldsymbol{\varepsilon} = d\boldsymbol{\varepsilon}^e + d\boldsymbol{\varepsilon}^p + d\boldsymbol{\varepsilon}^h$			
	$e_0 = \phi_0/(1-\phi_0)$ [(a)]	$\boldsymbol{e_0}$	0.72 0.88 0.667	1.93
Elastic strain increment:	$d\boldsymbol{\varepsilon}^e = -\frac{1}{3}d\varepsilon_v^e\mathbf{1} + d\boldsymbol{e}^e$ $d\varepsilon_v^e = \frac{dp'}{K}$, $K = \max\left\{\frac{(1+e)p'}{\tilde{\kappa}_i(s)}, K_{min}\right\}$ $\tilde{\kappa}_i(s) = \kappa_i(1+\alpha_i s)$ $d\boldsymbol{e}^e = \frac{d\boldsymbol{s}}{2G}$, $2G = \frac{3(1-\upsilon 2)}{(1+\upsilon)}K$	$\boldsymbol{\kappa_{i0}}$	0.13	0.2
		$\boldsymbol{\alpha_i}$	-0.021	0
		$\boldsymbol{v}$	0.2	0.2
		$\boldsymbol{K_{min}}$ **[MPa]**	20, [(c)]	1, [(c)]
Plastic strain increment:	$d\boldsymbol{\varepsilon}^p = d\Lambda\frac{\partial g}{\partial \boldsymbol{\sigma}}$ $f = q^2 - M^2(p'+p_s)(p_0-p')$ $g = \alpha q^2 - M^2(p'+p_s)(p_0-p')$ $p_0 = p_0^*$ $dp_0^* = \frac{1+e}{\lambda_0-\kappa_{i0}}p_0^* d\varepsilon_v^p$	$\boldsymbol{\alpha}$	0.5	0.5
		$\boldsymbol{p_0^*}$ **[MPa]**	10.338 4.626 10.338 [(d)]	0.153
		$\boldsymbol{\lambda_0}$	0.175 0.199 0.167	0.263 0.281 0.256
		$\boldsymbol{p_s}$ **[MPa]**	1.034 0.489 1.415	0.014
		$\boldsymbol{M}$	0.287 0.342 0.267	0.262
Hydraulic strain increment:	$d\boldsymbol{\varepsilon}^h = -\frac{1}{3}d\varepsilon_v^h\mathbf{1}$ $d\varepsilon_v^h = \frac{\kappa_s}{(1+e)(s+p_{atm})}ds$ $\kappa_s = \kappa_{s0}f^m(p',e)$ [(b)] $f^m(p',e) =$ $\begin{cases} 1 & \text{if } p' < p_{ref} \\ 10^{-20} & \text{if } p' > p_{swell}(e) \\ 1 - \frac{\ln p' - \ln p_{ref}}{\ln(\tilde{p}_{swell}(e)) - \ln p_{ref}} & \text{otherwise} \end{cases}$ $\log(\tilde{p}_{swell}(e)) = -4.741 + 4.117\cdot 10^{-3}\frac{\rho_s}{1+e} - 3.94\cdot 10^{-7}\left(\frac{\rho_s}{1+e}\right)^2$	$\boldsymbol{\kappa_{s0}}$	0.3	0.2
		$\boldsymbol{p_{ref}}$ **[MPa]**	0.1	0.08

[(a)] The initial void ratio is used as an input parameter to the modified BBM model. It should be set as to match the initial condition porosity.
[(b)] The function $f^m(p', e)$ is a feature developed at Clay Technology in which $\tilde{p}_{swell}(e)$ is obtained in MPa. $\tilde{p}_{swell}(e)$ is not equal to what was specified in the problem formulation. The function used in the SR-Site safety assessment simulations (see Åkesson et. al. 2010), was here adopted.
[(c)] When applying the vertical load in Case 1, a value of 200 MPa was used for B and PS materials.
[(d)] p_0^* = 14.445 MPa was obtained for Case 5. For convergency, the Base Case value was used instead.

2.3.3 Liquid phase

The liquid **phase density** is given by,

$$\tilde{\rho}_l(p_l, T) = 1002.6\exp(4.5\cdot 10^{-4}(p_l - 0.1) + 3.4\cdot 10^{-4}T)\ [\mathrm{kg/m^3}]\,, \qquad (2\text{-}4)$$

and the **liquid phase viscosity** is given by,

$$\tilde{\mu}_l(T) = 2.1 \cdot 10^{-12} \exp\left(\frac{1808.5}{273.15 + T}\right) \text{ [MPa} \cdot \text{s]} . \tag{2-5}$$

In the two expressions above liquid pore pressure is given in MPa and temperature in °C.

2.3.4 Gas phase

The gas phase consists of two constituents water vapor and dry air. The total gas pressure, p_g, is given by the sum of the constituents' partial pressures, i.e., $p_g = p_g^w + p_g^a$. The models for **water gas pore pressure**, p_g^w, is given by,

$$\tilde{p}_g^w(T) = 13607 \exp\left(\frac{-5239.7}{273.15 + T}\right) \text{ [MPa]} , \tag{2-6}$$

and the **air gas pore pressure**, p_g^a, are indirectly given by,

$$\tilde{\theta}_g^a\left(T, p_g - p_g^w\right) = \frac{M_a}{R} \frac{1}{273.15 + T} \left(p_g - p_g^w\right) \left[\frac{\text{kg}}{\text{m}^3}\right]. \tag{2-7}$$

In the two expressions above pressures are given in MPa and temperature in °C.

3 Comments regarding the model setup

3.1 Swelling pressure curves

The simulations in this work have been utilizing the swelling pressure curve defined in Table 2-9. This is identical to the one used when performing the simulations for the SR-Site safety assessment Åkesson et al. (2010). It does not, however, agree well with the one presented in the problem formulation documentation which were taken from Svensson et al. (2017). The two swelling pressure curves are shown together in Figure 3-1 where the SR-Site curve is significantly lower than the newer curve.

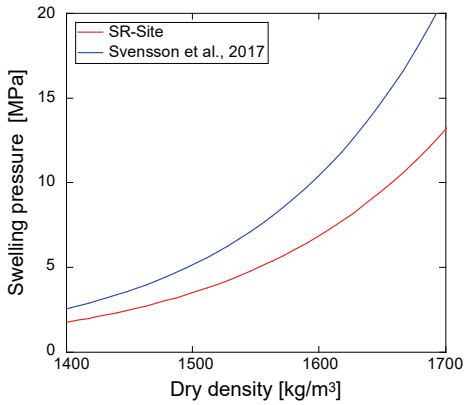

Figure 3-1. Swelling pressure curves. The SR-Site swelling pressure curve used in this work and the swelling pressure curve from the problem formulation documentation (Svensson et al. 2017).

This large difference was unfortunately not realized at the time performing the simulations. At that time, however, the possibility to change the swelling pressure curve in Code_Bright was quite troublesome. The parameter values had to be specified in the source code and a new version of Code_Bright had to be compiled to obtain an executable program. As this procedure has not been carried out for some years it would have needed some time for starting it up again. Thus, it could have been done but was troublesome. Recently, however, an option has been added to the code where the parameter values is defined in the graphical interface which facilitates changes in the swelling pressure curve significantly.

There has been an ongoing discussion of what swelling pressure curve to use. When comparing different data sets the difference can be rather significant. More recent data sets, from tests with samples of smaller height to radius ratio, suggest that older data sets might underestimate swelling pressures. Thus, the discrepancy in presented in Figure 3-1 comes from using different data sets when calibrating the swelling pressure curves.

3.2 Calibrating BBM for the buffer materials

The parameter set in Sandén et al. (2020) was used as a starting point for the current setup. The elastic parameters were then adjusted to be more in line with what was suggested in Åkesson et al. (2010).

The plastic parameters $p_0{}^*$, M and p_s were obtained by using a similar strategy as described in Åkesson et al. (2010). This is based on identifying three stress states at yielding ($f = 0$):

$$\begin{aligned} (p'_A, q_A) &= (p_s + 2p_{swell}, 0), \\ (p'_B, q_B) &= (p_{swell}, q_f), \\ (p'_C, q_C) &= (-q_f/6\,, q_f/2), \end{aligned} \tag{3-1}$$

and insert these into the yield function,

$$f = 0 = q^2 - M^2(p' + p_s)(p_0 - p')\,, \tag{3-2}$$

to obtain three equations from which the plastic parameters can be obtained.

For the B material, experimentally motivated functions for swelling pressure $\tilde{p}_{swell}(e)$ and von Mises stress at failure $\tilde{q}_f(p') = \tilde{q}_f(\tilde{p}_{swell}(e))$ were used to define p_{swell} and q_f. Both functions are described in Åkesson et al. (2010), $\tilde{p}_{swell}(e)$ was defined in Table 2-9 and

$$\tilde{q}_f(p') = 0.5{p'}^{0.77}, \tag{3-3}$$

where the unit is MPa. The void ratio used when calculating p_{swell} was taken as the radially homogenized void ratio, e_H.

For the PS material, $\tilde{p}_{swell}(e)$ was also used but the von Mises stress at failure was instead given by,

$$q_f = M(p_{swell} + p_s)\,. \tag{3-4}$$

This comes from the strategy used for including wall friction as a property of the PS-material. Since the friction angle $\phi = 7.2°$ was given, M is obtained by,

$$M = \frac{6\sin\phi}{3 - \sin\phi}. \tag{3-5}$$

The void ratio used when calculating p_{swell} was here taken as the initial void ratio, e_0.

The value of the plastic stiffness λ_0 is obtained from,

$$\lambda_0 = -\frac{\tilde{p}_{swell}(e_H)}{\frac{d}{de_H}\tilde{p}_{swell}(e_H)}, \tag{3-6}$$

for the B-material, and

$$\lambda_0 = -\frac{e_0 - e_H}{\ln\left(\tilde{p}_{swell}(e_0)\right) - \ln\left(\tilde{p}_{swell}(e_H)\right)}, \tag{3-7}$$

for the PS-material.

To get convergency for the C5 simulation, the p_0 value for the B-material was set according to the BC setting instead of the value obtained by using the scheme above.

Axisymmetric plane strain 1D-models of a horizontal section of the simplified KBS-3V system were used to check the mechanical process, see Figure 3-2, and the homogenisation of the B and pellet filled slot, see Figure 3-3. The mechanical process, in terms of the evolution of the pair (effective pressure, void ratio), was evaluated in relation to experimentally motivated swelling curve (given by the expression in Table 2-9) and compression curve (given by multiplying the expression in Table 2-9 by 2). The homogenisation was evaluated by observing the appearance of the final dry density profile at the interface between the B and PS materials.

The parameter p_{ref} was calibrated as to obtain a response ending up between the swelling and compression curve and also as to obtain a "smooth" appearance of the final dry density profile at the transition between B and PS materials.

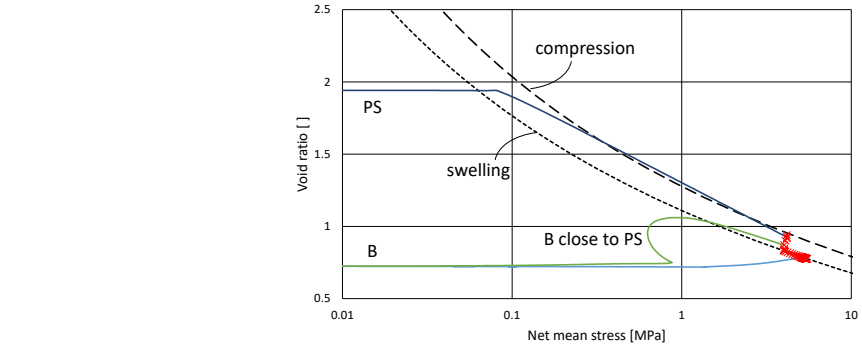

Base Case

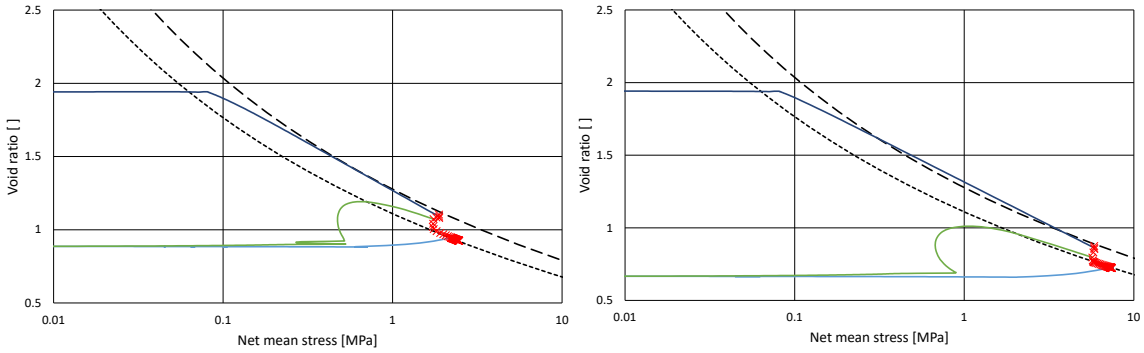

Case 4 Case 5

Figure 3-2. Mechanical evolution (p',e) in the 1D models. The swelling curve is generated by using the expression in Table 2-9 and the compression curve by multiplying the same expression with 2.

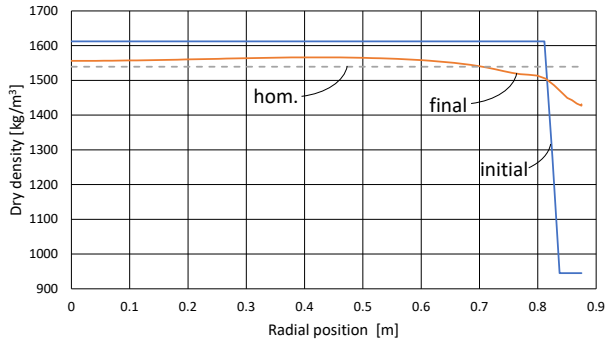

Base Case

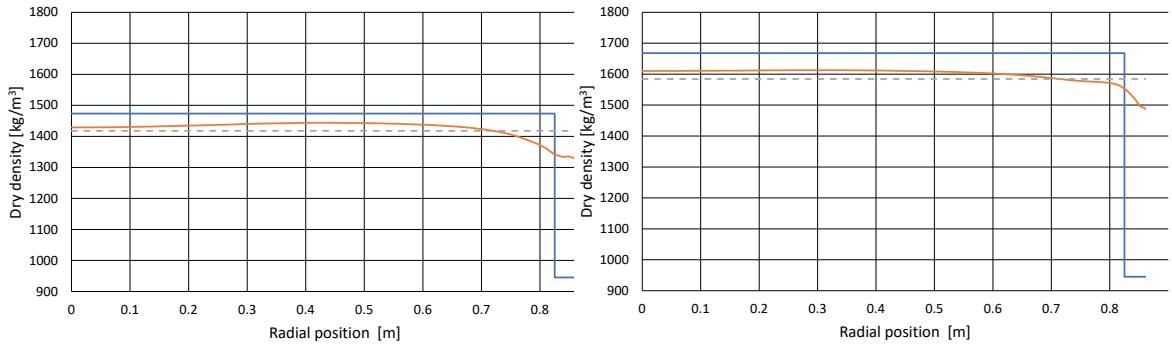

Case 4 Case 5

Figure 3-3. Dry density profiles obtained in the 1D models.

3.3 Hydraulic representation of buffer materials

3.3.1 Retention

Van Genuchten retention curves given by,

$$\widetilde{S}_l(p_l) = \left(1 + \left(\frac{p_g - p_l}{P_0}\right)^{\frac{1}{1-\lambda}}\right)^{-\lambda}, \tag{3-8}$$

were calibrated by using λ as a fitting parameter, as to get a suitable curve shape, and P_0 given by the initial state. The retention curves are shown in Figure 3-4.

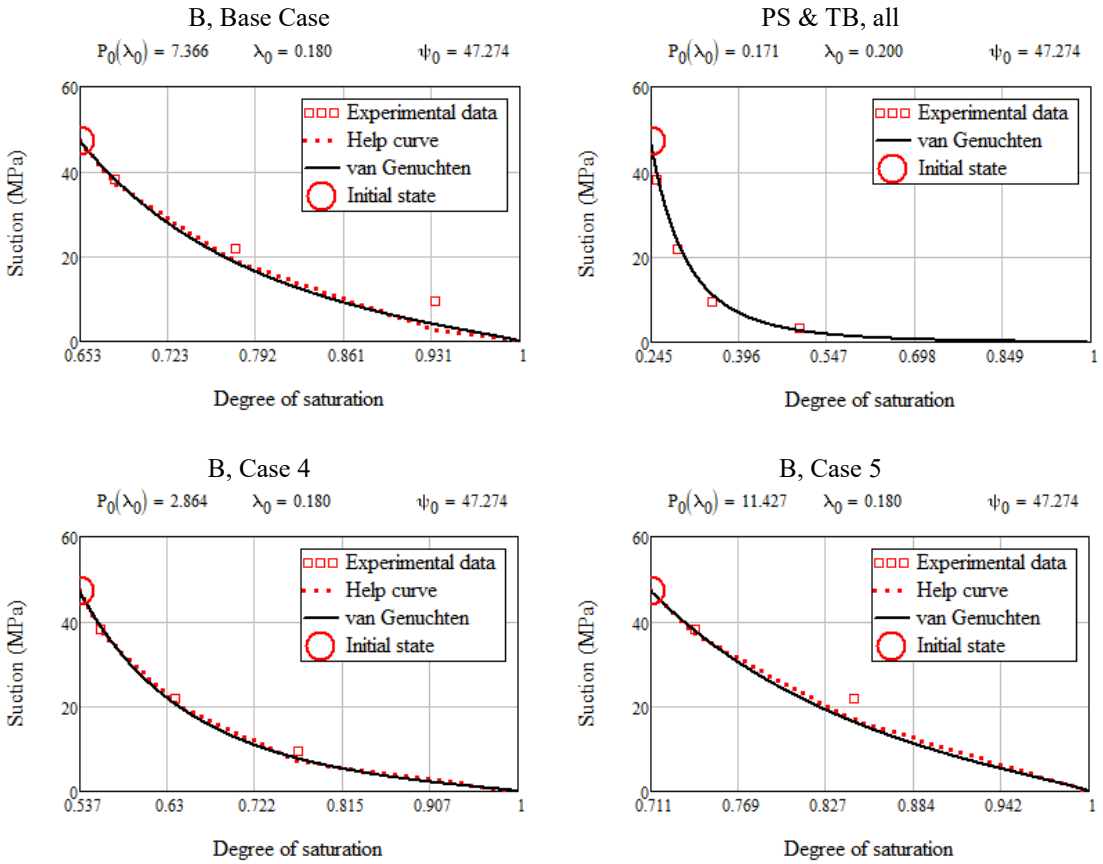

Figure 3-4. Retention curves for the B, PS, and TB materials. The parameter values for P_0 [MPa] and λ [-] are given above the graphs. ψ_0 [MPa] denotes the initial suction.

For the B material "help curves" were obtained by using experimental RH-water ratio data for free conditions (Dueck 2004), and the relation: help curve = suction at free conditions – swelling pressure. The swelling pressure was assumed to be linearly increasing from zero at the initially unsaturated state to the fully saturated state where its magnitude equals the suction at the water ratio corresponding to fully saturated conditions. The B-material retention curve was then fitted to this help curve. For the PS materials a help curve was not used since it did not give much additional information, the retention curve was instead fitted close to the experimental data points.

3.3.2 Initial setting of the porosity dependent permeability

Experiments show that the permeability of bentonite clay is dependent on dry density. The experimental data can be fitted using different expressions, and in Åkesson et al. (2010) the expression,

$$\tilde{k}(e) = k_{ref}\left(\frac{e}{e_{ref}}\right)^{\eta}, \tag{3-9}$$

given as a function of void ratio, was suggested to be equipped with the parameter set $\{k_{ref} = 2.4 \cdot 10^{-20}$ m/s, $e_{ref} = 1$, $\eta = 5.33\}$.

The function given above was used as a "target function" when evaluating a suitable value of the parameter b in the function,

$$\tilde{k}_{in}(e) = k_{ref} \exp\left(b \left(\frac{e}{1+e} - \frac{e_{ref}}{1+e_{ref}} \right) \right), \tag{3-10}$$

available in Code_Bright. It was found that $b = 21.764$ gave a good agreement between the target function and the Code_Bright expression.

3.3.3 Diffusivity analysis, updated porosity dependent permeability

The applicability of the parameter setting of the hydraulic description can be evaluated by calculating a moisture diffusivity, using the parameter values, and compare this with the result obtained from fitment against water uptake tests, see Sellin et al. (2017). Results obtained from fitment against water uptake tests for compacted bentonite samples are shown in Figure 3-5 and as can be seen, the MX-80 data for the lower void ratio ($e = 0.7$) ends up at about $4 \cdot 10^{-10}$ m^2/s and the higher void ratio ($e = 1.0$) about $3 \cdot 10^{-10}$ m^2/s.

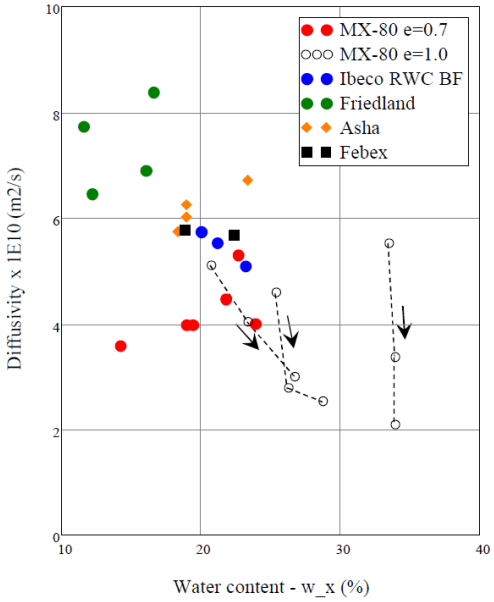

Figure 3-5. Diffusivity values evaluated from water-uptake tests. Part of Figure 7-1 in Sellin et al. (2017).

The moisture diffusivity can be calculated from the expression,

$$\tilde{D}(\phi, S_l) = \frac{\tilde{k}_{in}(\phi)\tilde{k}_{rl}(S_l)}{\phi \mu_l} \left(\frac{d\tilde{S}_l}{dp_l}(S_l) \right)^{-1}, \tag{3-11}$$

where k_{ref} and n in $\tilde{k}_{in}(\phi)$ and $\tilde{k}_{rl}(S_l) = S_l^{\,n}$, respectively, were used for fitting so that a suitable magnitude and dependence on degree of water saturation was obtained.

When evaluating a moisture diffusivity for the B-material a value of $4 \cdot 10^{-10}$ m^2/s was used as a reference value. The result from the calibration is shown in Figure 3-6, both in terms of moisture diffusivity and hydraulic conductivity.

As shown in Figure 3-5 , when evaluating a moisture diffusivity for a water uptake test containing a lower density sample ($e = 1.0$) a value of $3 \cdot 10^{-10}$ m^2/s was found suitable. The result form the PS material calibration is shown in Figure 3-7, both in terms of moisture diffusivity and hydraulic conductivity. The selected low value for the exponent, n, could be considered a "trick" as to obtain a more representative initial water uptake for the present material structure. The resulting low flow

resistance at low degrees of saturation is expected to be relevant for a material with large macro voids, which is the case for a pellet filled slot at dry conditions.

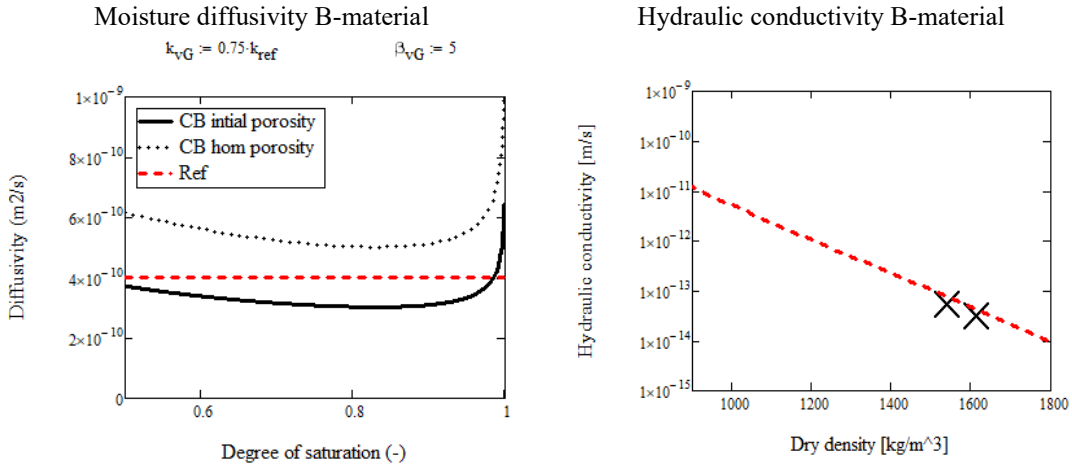

Figure 3-6. Moisture diffusivity and hydraulic conductivity for the B material with $k_{ref} = 1.8 \cdot 10^{-20}\ m/s$ and $n = 5$. The crosses indicate the resulting conductivities at the initial state and a homogenized system.

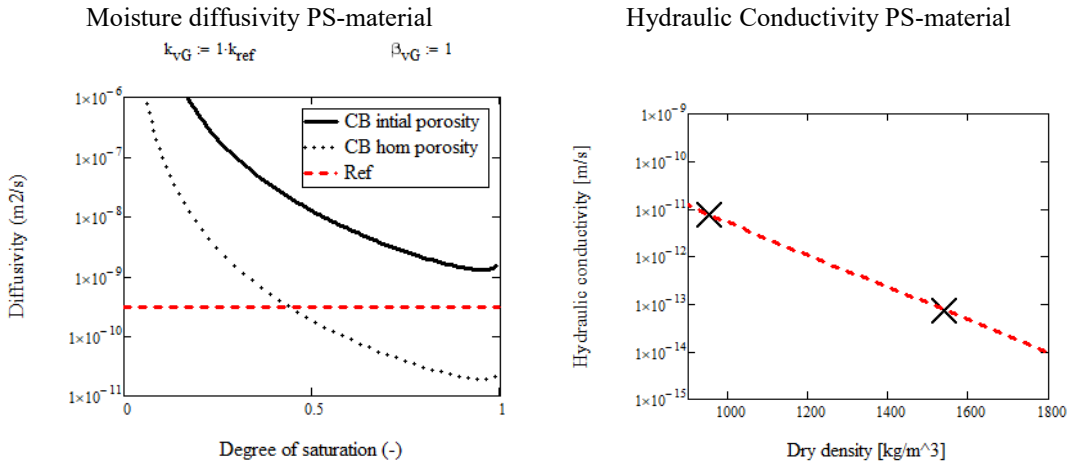

Figure 3-7. Moisture diffusivity and hydraulic conductivity for PS material $k_{ref} = 2.4 \cdot 10^{-20}\ m/s$ and $n = 1$. The crosses indicate the resulting conductivities at the initial state and a homogenized system.

3.4 Mechanical representation of the TB

In the assignment specification the vertical reaction force from the TB is, for all cases except C1, given in terms of a spring constant, k, given in MPa/m such that the vertical force F_v over an area A becomes,

$$F_v = A\, k\, u_v\,, \tag{3-12}$$

where u_v is the heave of the top surface of the buffer. Since updated coordinates are selected in Code_Bright, to make the formulation better suited for significant deformation, the vertical strain component is given by,

$$\varepsilon_v = \frac{u_v}{L_{TB} - u_v}\,, \tag{3-13}$$

where L_{TB} denotes the height of the TB component in the reference configuration. To represent the TB-material in Code_Bright, a linear elastic material ($\sigma_v = E_{TB}\varepsilon_v$) is utilized which gives that the vertical force F_v can be expressed as,

$$F_v = AE_{TB}\varepsilon_v = AE_{TB}\frac{u_v}{L_{TB} - u_v}\,, \tag{3-14}$$

which results in the relation,

$$k = E_{TB}\frac{1}{L_{TB} - u_v}. \tag{3-15}$$

Thus, if $u_v \ll L_{TB}$ then,

$$E_{TB} \approx kL_{TB}\,. \tag{3-16}$$

In order to decrease the stiffening effect on the solution from the stress concentration at the "corner", where B, PS and TB meet, the vertical column above the PS was in some cases allotted a softer TB-material. If calculating a combined stiffness of two parallel TB-materials 1 and 2 with stiffness E_1 and E_2, and sectional areas A_1 and A_2, we obtain,

$$E_{TB} = \frac{A_1}{A}E_1 + \frac{A_2}{A}E_2\,, \tag{3-17}$$

from which E_1 or E_2 can be calculated.

A new feature of Code_Bright, when prescribing mechanical boundary conditions, was utilized to represent the TB in some cases. The new boundary condition could represent a linear spring with stiffness k_{bc} [MPa/m] according to,

$$\sigma_{bc} = k_{bc}\,u_{bc}\,. \tag{3-18}$$

If combined in serial with the linear elastic material with elastic modulus E_{TB}, and knowing the total spring constant k, the spring constant of the boundary condition is obtained from,

$$k_{bc} = \frac{k}{1 - \frac{k(L_{TB} - u_v)}{E_{TB}}}\,. \tag{3-19}$$

4 Results from the first set of simulations

In this chapter the results requested for the first set of simulations, see Table 1-1, are given. Before this, however, the mechanics of the BC model is evaluated. The evaluation is made by comparing the final mechanical state of the simulation against swelling and compression pressure curves as well as stress state at failure. The effect from the mechanical binding at the corner where B, PS, and TB materials meet, and an effective friction angle are also studied.

4.1 Evaluation of the Base Case simulation

The mechanical final state in the buffer (except the upper most 5cm in the PS, see discussion below) is evaluated by comparing the obtained pairs in effective pressure -void ratio (p', e), to swelling and compression curves. The swelling pressure curve is defined in Table 2-9 and the compression curve is defined as twice the swelling pressure curve, i.e., $p_{comp}(e) = 2p_{swell}(e)$. The data in Figure 4-1 indicates that the final mechanical state in the buffer is appropriate. It is noticeable that due to the heave, a significant part of the B material has swollen beyond the initial homogenised void ratio, indicated by the black X, used when calibrating the plastic parameters in the B material model. This is discussed below.

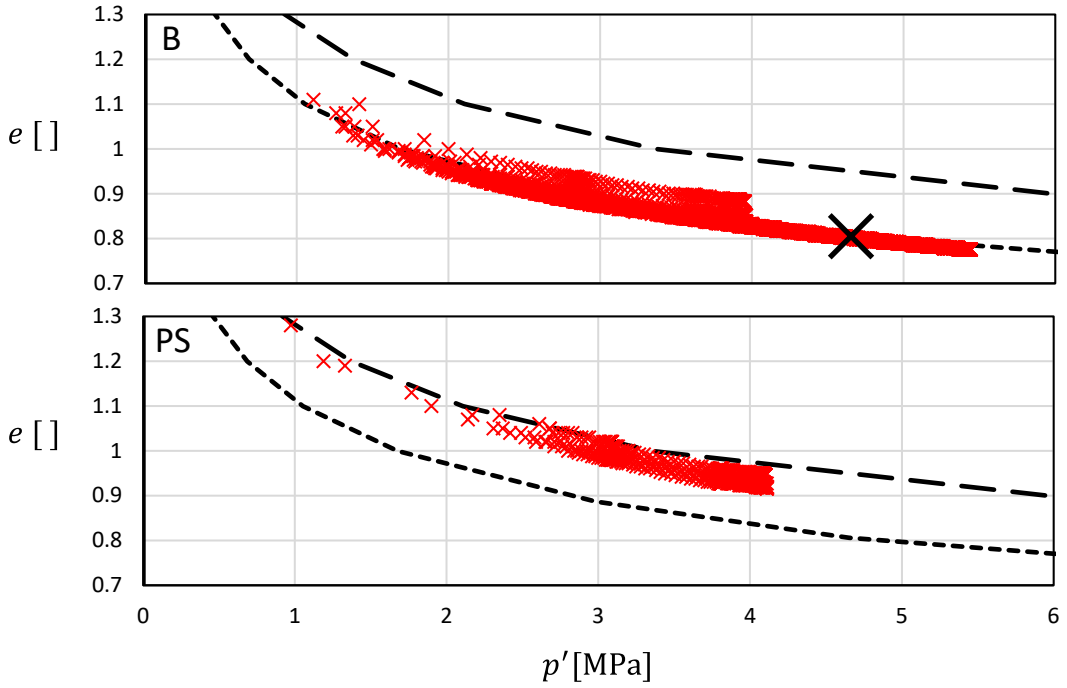

Figure 4-1. Final mechanical state in terms of (p', e) (red crosses) for B and PS components, upper and lower graph, respectively, together with compression and swelling pressure curves (black long and short hatched lines, respectively). The swelling pressure curve is defined in Table 2-9. The compression curve is twice the swelling pressure curve. In the upper graph X indicates the pair (homogenised initial state void ratio, swelling pressure).

The final stress state is evaluated by studying pairs of effective pressure and a deviatoric stress invariant (p', q). Figure 4-2 shows the obtained stress states in the B and pellet filled slot separately in the upper and lower graph respectively. Together with the model data, Figure 4-2 also shows the function $\tilde{q}_f(p')$, describing the relation between the deviatoric stress invariant at failure and the effective pressure (solid black line), the initial flow surface (dotted black line), the critical state line obtained from $M(p' - p_s)$ (grey line), and the pair (p_{swell}, q_f) at the initial state (black circle).

As can be seen in Figure 4-2, most points in the model have stress states (p', q) which are below $\tilde{q}_f(p')$ and $M(p' - p_s)$, i.e. $q < \tilde{q}_f(p')$ and $q < M(p' - p_s)$. There are, however, points in the B material where $q > \tilde{q}_f(p')$ and $q > M(p' - p_s)$. This does not indicate that the simulation is wrong, BBM allows for stress states (p', q) where $q > M(p' - p_s)$. With the current setup of the B material, using the initial homogenised void ratio when calibrating the plastic parameters, these states can be

expected since BBM does not in general contract its yield surface when the material undergoes swelling.

One could argue that the plastic parameters should be calibrated using another "target void ratio" for the B material, i.e., larger than the initially homogenised void ratio. The range in void ratio data, shown in Figure 4-1, is wide and what target void ratio to select is, however, not obvious. Furthermore, the range would be different for different cases and the setup would become more "process dependent" which indicates that the material model itself might not be a perfect candidate for a general representation of bentonite clay.

As for the PS material, there are only a few points for which the stress state (p', q) has $q > M(p' - p_s)$, for most points $q \leq M(p' - p_s)$. Thus, the PS material behaves as intended. The situation differs from that of the B material in that the plastic parameters were calibrated using the initial high void ratio of 1.93 and the mechanical process for the PS material in large is dominated by compression and, for points close to the buffer top, significant shearing. The inner workings of the material model are more "uniform" for the PS as compared to the B material which makes it easier to set up properly.

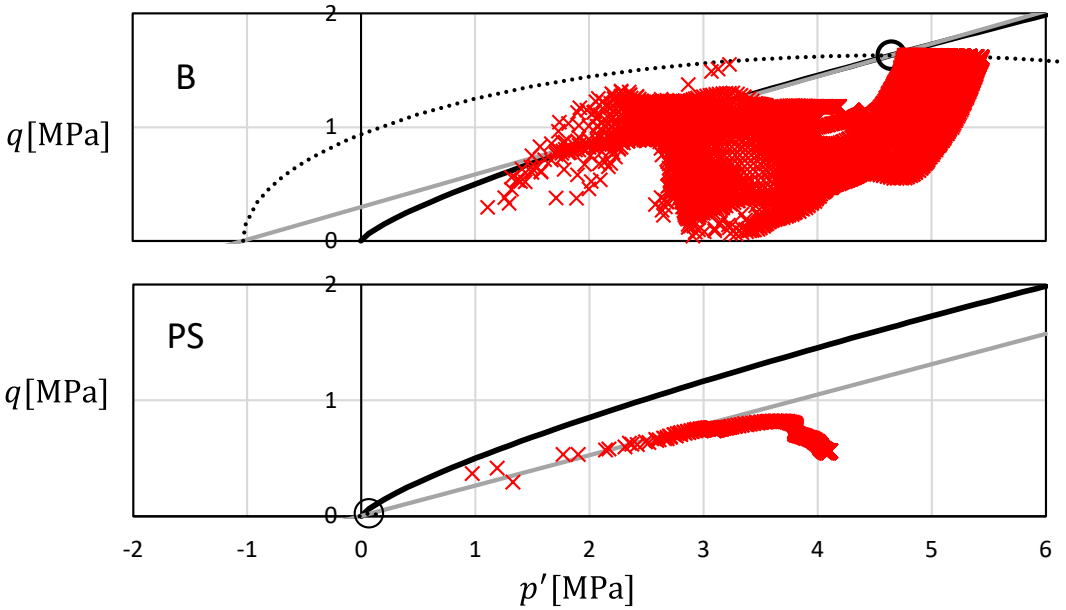

Figure 4-2 Final stress states (p', q) (red crosses) together with, $\tilde{q}_f(p')$ (solid black line), $M(p' - p_s)$ (solid grey line), the initial flow surface, $f_0 = 0$ (dotted black line) and initial (p_{swell}, q_f) (black circle). The results for the B and PS components are shown in the upper and lower graph, respectively.

It is expected that the presently idealised problem formulation deviates from an "ideal problem formulation" (agreeing better with reality) at the corner, where B, PS and TB meet, due to the assumption of perfect bonding between the materials with significant difference in mechanical properties. Trying to evaluate this effect, the vertical boundary node forces were studied over the PS boundary for the BC model. The node forces at the top 5 cm along the PS boundary stood out with evolutions deviating from the trends in the other nodes. This could partly come from using "cross-triangle" elements, introduced to obtain convergence.

To evaluate how the conditions at the corner affect the solution, comparison of ratios between different sums of vertical node forces is made. The sums are:

- $\sum F_{upper}$: The sum of vertical node forces from 0 cm to 5 cm from the top along the PS boundary,
- $\sum F_{lower}$: The sum of vertical node forces from 5 cm to 10 cm from the top along the PS boundary,
- $\sum F$: The sum of all vertical node forces along the PS boundary.

As shown in Figure 4-3, the upper interval force constitutes between 10 % (initially) to 2.5 % (at the end of the simulation) of the total and the lower between 3 and 1.5 % of the total. The vertical force counteracting the vertical buffer swelling is therefore likely to be overestimated in the simulation. The simulation could therefore underestimate heave and reaction pressure.

If assuming the reaction force of the upper 5 cm interval having similar contribution to the total vertical force as compared to the next 5 cm interval, a total vertical force along PS, $\sum F - \sum F_{upper} + \sum F_{lower}$, is estimated to be 95 to 99 % of the one in the current simulation, Figure 4-3.

It should be said that the evaluation made above is crude. It may be that the perfect bond between the three materials also introduce local phenomena such as shear band formation which affect the global mechanical response of the system.

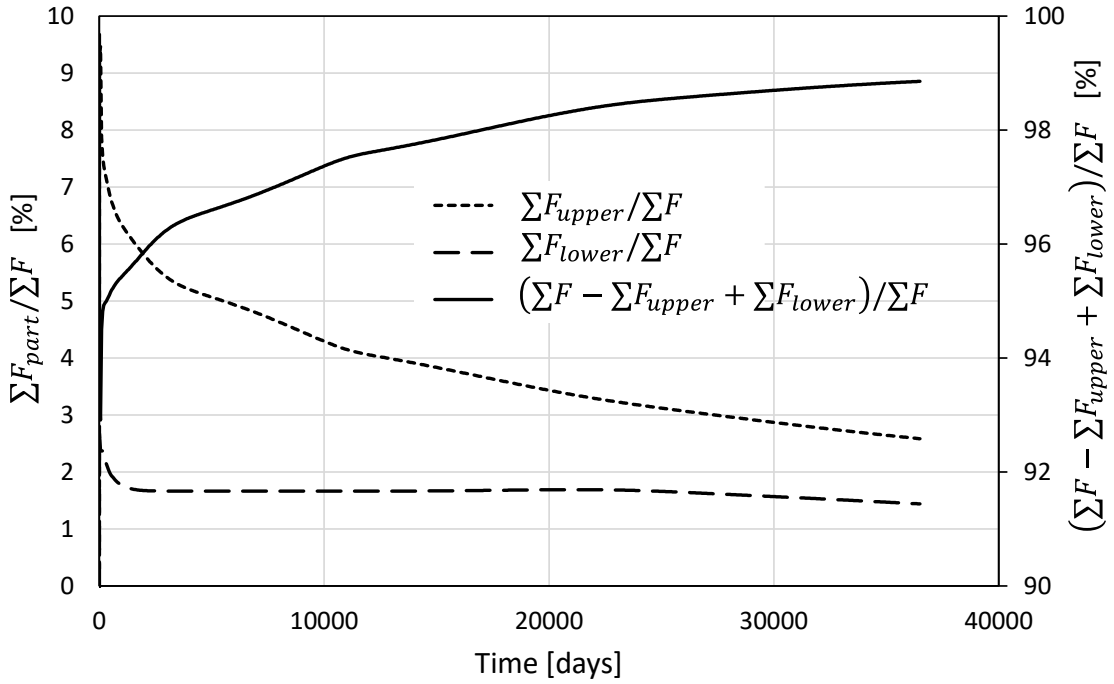

Figure 4-3. Base Case simulation evaluation. Calculated ratios between the sum of node forces of two chosen node subsets (upper and lower) and the sum over all nodes, left scale. An estimation of the effect from the corner conditions on the vertically resistive force, right scale.

In the simulation, resistance against vertical deformation in the material close to the deposition hole wall is represented by the PS material model, the modified version of BBM. If instead assuming a Mohr – Coulomb failure condition, without cohesion, an "effective friction angle", $\mathrm{atan}(\tau/\sigma)$, can be calculated from the normal (=*r*adial) and tangential (=*v*ertical) node forces ($\tau/\sigma = dF_r/dF_v$) along the PS boundary.

In Figure 4-4, the evolution of this quantity is shown for the nodes below 7.95 m height along the PS boundary in the BC model. The top-most 5 cm was not included due to the issues described above. Some nodes have values above the specified 7.2 °. This is what to expect since BBM allows for stress states generating effective friction angles larger than what is given by the parameter M. In general, however, the evaluated effective friction angle is at or below the specified value.

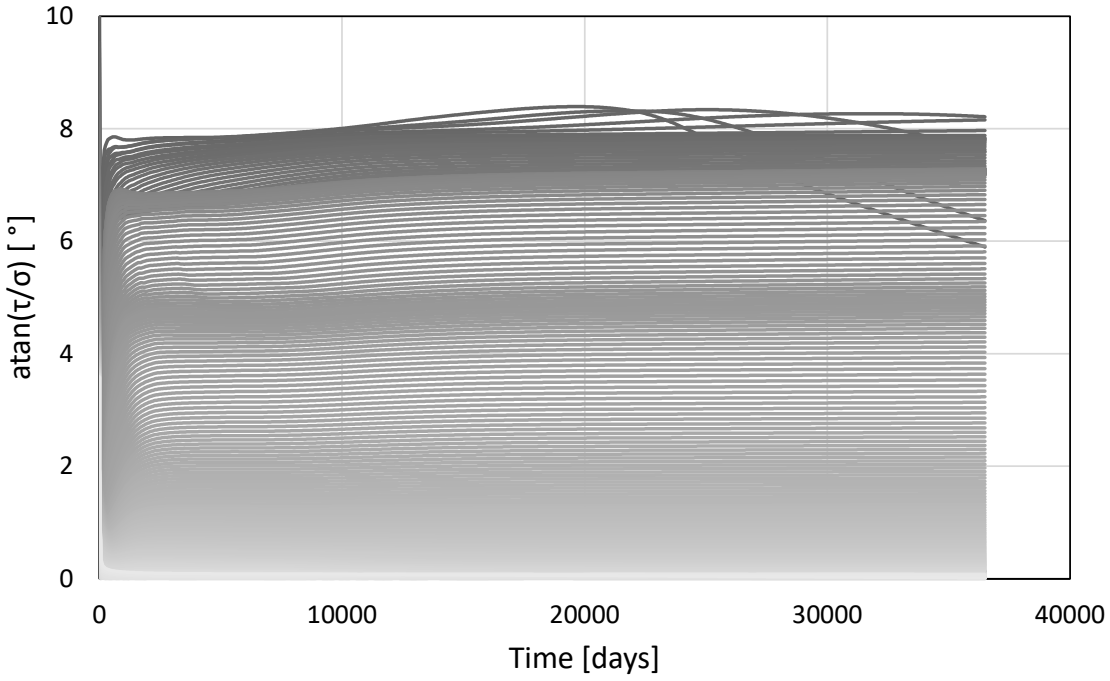

Figure 4-4. An "effective friction angle", $atan(\tau/\sigma) = atan(dF\_r/dF\_v)$, evaluated for all nodes at the lower 7.95 m of the PS boundary in the Base Case model.

4.2 Requested results from the first set of simulations

The following definitions have been used when reporting results from the simulations:

- Heave: $heave = \frac{V_{swell}}{A}$
- Reaction pressure: $p^R = \frac{-F_v}{A}$
- Volume generated by swelling: $V_{swell} = \int u_v \, dA$ over B & PS top surface
- Vertical reaction force: $F_v = \int \sigma_v \, dA$ over TB top surface
- Deposition hole cross section area: $A = \pi \, 0.875^2$ m^2

Below follows the results which were requested in the assignment description. Compilations of heave and reaction pressure are first given in Table 4-1. Then follows dry density profiles along the symmetry axis and rock wall boundary together with iso-maps of dry density in Figure 4-5 to Figure 4-10 where the results are mapped on the undeformed geometry.

Table 4-1. Compilation of heave and reaction pressure.

Case	$heave$ [m]	p^R [MPa]
Base Case	0.109	2.04
Case 1	0.129	1.50
Case 2	0.430	0.45
Case 3	0.141	2.67
Case 4	0.065	1.26
Case 5	0.132	2.46

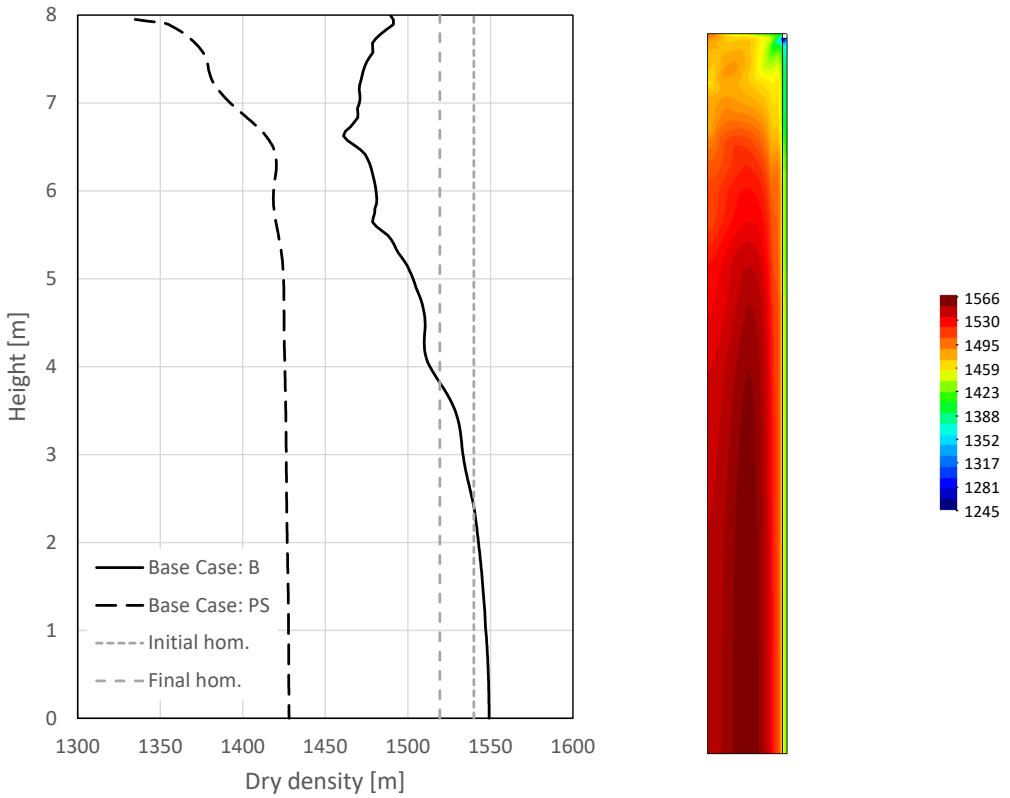

Figure 4-5. Base Case: Vertical profiles of the dry density field along the symmetry axis and rock wall boundary together with the averaged values in the initial and final configurations (left). Map over the dry density field at the final state (right).

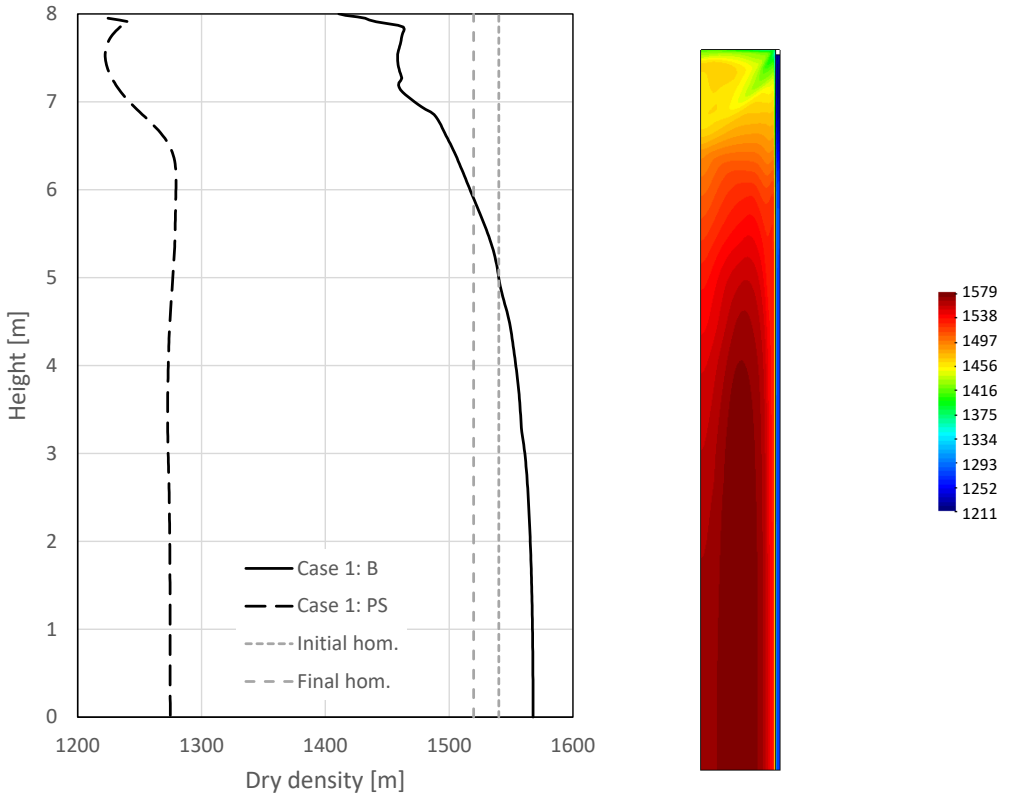

Figure 4-6. Case 1: Vertical profiles of the dry density field along the symmetry axis and rock wall boundary together with the averaged values in the initial and final configurations (left). Map over the dry density field at the final state (right).

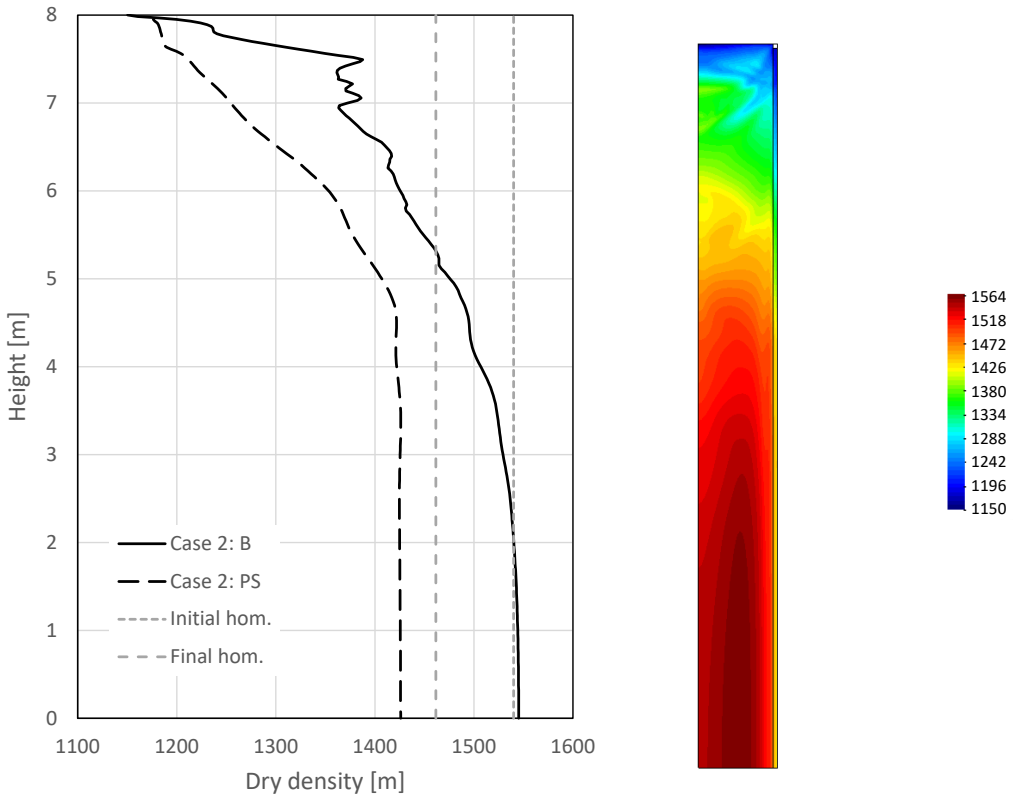

Figure 4-7. Case 2: Vertical profiles of the dry density field along the symmetry axis and rock wall boundary together with the averaged values in the initial and final configurations (left). Map over the dry density field at the final state (right).

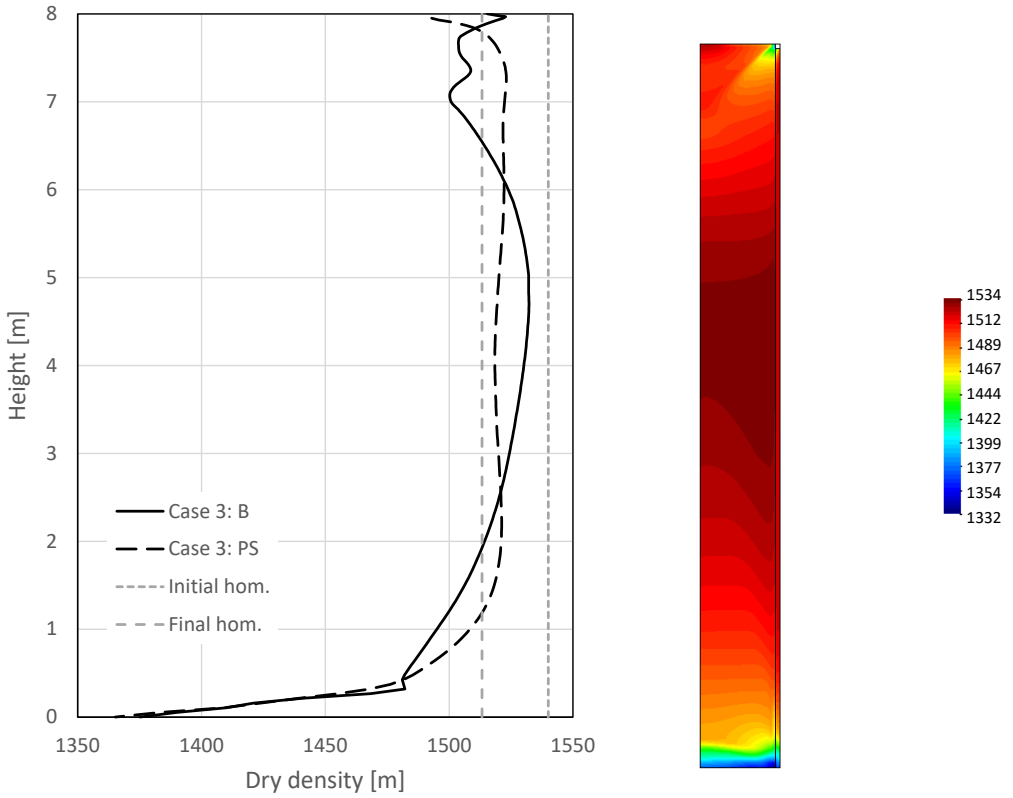

Figure 4-8. Case 3: Vertical profiles of the dry density field along the symmetry axis and rock wall boundary together with the averaged values in the initial and final configurations (left). Map over the dry density field at the final state (right).

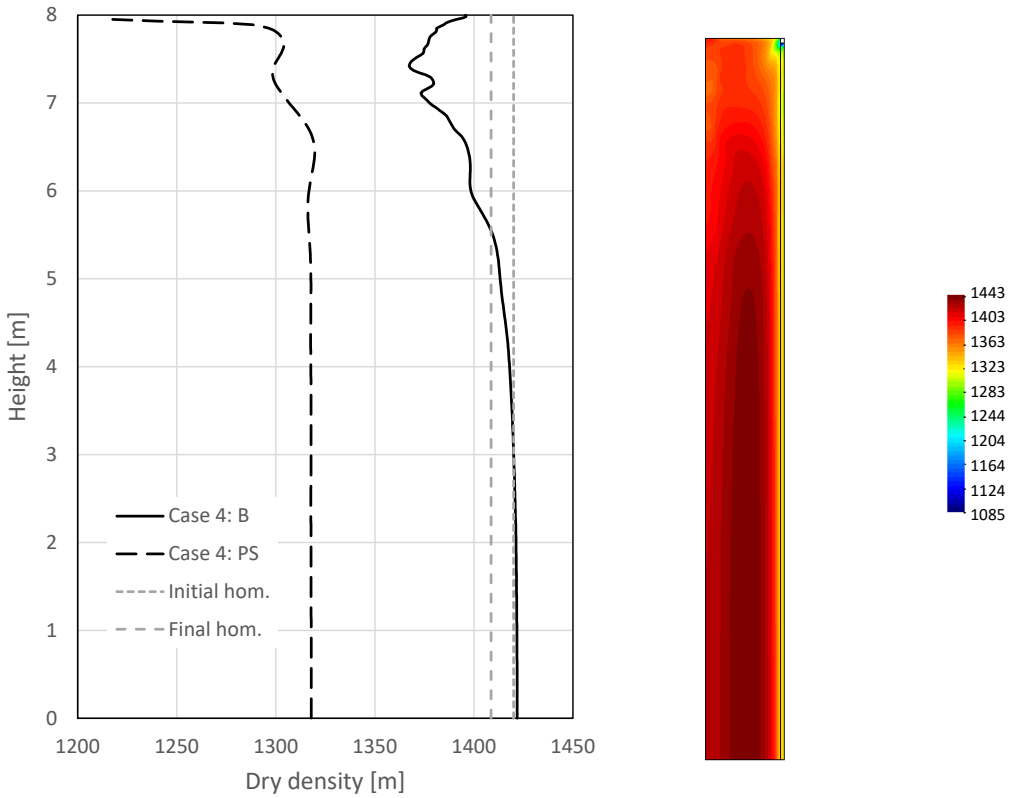

Figure 4-9. Case 4: Vertical profiles of the dry density field along the symmetry axis and rock wall boundary together with the averaged values in the initial and final configurations (left). Map over the dry density field at the final state (right).

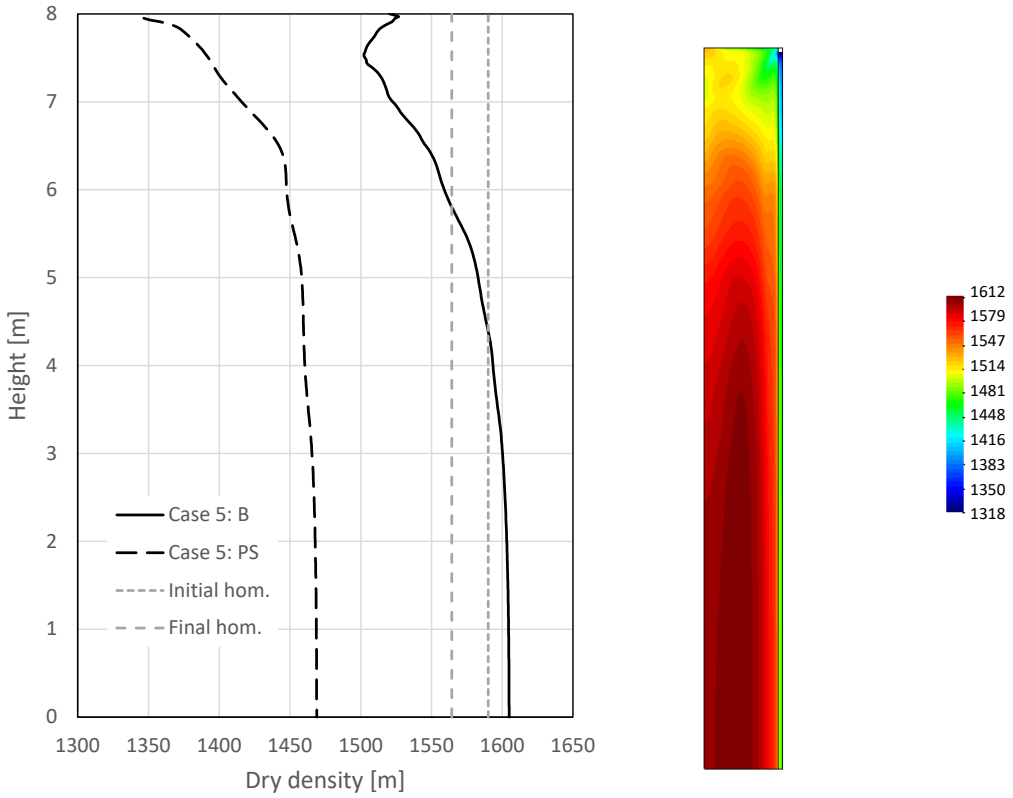

Figure 4-10. Case 5: Vertical profiles of the dry density field along the symmetry axis and rock wall boundary together with the averaged values in the initial and final configurations (left). Map over the dry density field at the final state (right).

5 Results from the second set of simulations

In this chapter follows results from the second set of simulations, see Table 1-2. Before these are given, however, the changes made to the BC and C2 models, used in the first set, are described and mesh dependency is studied.

The BC and C2 were revisited when applying different friction angles in the PS material governing the wall friction. The original friction angle was 7.2° and the new values were 5° and 1°. When changing the friction angle, two parameters in the PS material was changed according to Table 5-1. In addition to using the prescribed friction angles, both cases were also simulated assuming frictionless conditions along the PS vertical boundary using roller boundary conditions. Thus, the second set of simulations was {BC:7.2°, BC:5°, BC:1°, BC:rollers, C2:7.2°, C2:5°, C2:1°, C2:rollers}.

Table 5-1. Compilation friction angle and corresponding plastic parameters in the PS material.

	$\phi = 7.2°$	$\phi = 5°$	$\phi = 1°$
p_s [MPa]	0.014	0.013	0.011
M	0.262	0.180	0.0351

In this second take on the BC and C2 models, the representation of the TB was improved by using new combinations of linear elastic TB materials and spring boundary conditions. The elastic parameters are given in Table 5-2 and the spring stiffness used in the boundary condition was 180 MPa/m and 1.3 MPa/m, in the BC and C2 simulations, respectively.

Table 5-2. Linear elastic model and parameter values.

Total strain increment	$d\boldsymbol{\varepsilon} = d\boldsymbol{\varepsilon}^e$	**Parameter**	**TB**	**TB$_{soft}$**
Elastic strain increment:	$d\boldsymbol{\varepsilon}^e = -\frac{1}{3}d\varepsilon_v^e\mathbf{1} + d\boldsymbol{e}^e$ $d\varepsilon_v^e = \frac{dp'}{K}, K = \frac{E}{3(1-2\upsilon)}$ $d\boldsymbol{e}^e = \frac{d\boldsymbol{s}}{2G}, 2G = \frac{E}{1+\upsilon}$	E [MPa]	BC: 22.248 C2: 1	BC: 2 C2: -
		υ	0.0001	0.0001

5.1 Mesh dependency study

Mesh dependency was studied for the C2:7.2° case. Figure 5-1 shows the heave and reaction pressure obtained for three different mesh densities (coarse, mid, fine), where the number of elements over the sides of a component were doubled between the meshes. For reference, the first set C2 result, where the mid mesh density were used, is also included. The specified TB representation (with a spring stiffness of 0.75 MPa/m) as well as the one used in the simulation are also included in the graph.

For the mid mesh density, which is the one used in the study, the result has more or less converged towards the result of the fine mesh density. This indicates that the model using the mid mesh density produce results with high enough accuracy for the present analysis.

The improvement of the TB representation in the updated model within the second set is seen when comparing the first set results to the mid mesh density results, where the latter is closer to the specified TB representation. The difference between the simulated TB curve and the obtained results

is likely due to that the TB material was calibrated assuming uniaxial conditions, which is not generally true for the simulations.

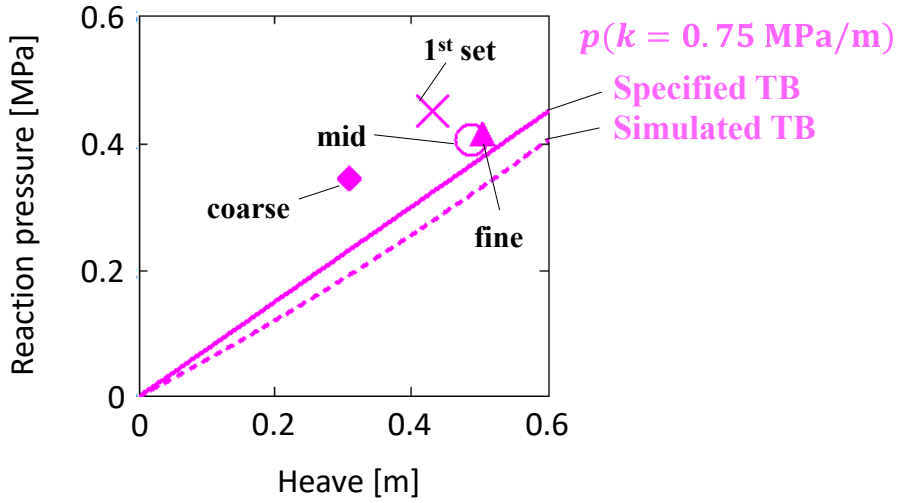

Figure 5-1. Compilation of FE-results for C2:7.2° using different mesh densities together with functions describing TB representations. The C2 case from the 1st set of simulations is also included.

5.2 Requested results from the second set of simulations

Below follows the results which were requested in the assignment description. A compilation of heave and reaction pressure is given for all simulations relevant for the second set of cases in Table 5-3. Then follows the dry density profiles along the symmetry axis and the vertical rock wall boundary together with iso-maps of dry density for BC:5°, BC:1°, and C2:5° in Figure 4-5 - Figure 4-10. The profile and iso-map for C2:1° is not shown since the obtained solution is of poor quality.

Table 5-3. Compilation of heave and reaction pressure relevant for the second set of cases.

Case	*heave* [m]	p^R [MPa]	Comment
Base Case, 7.2° 1st set	0.109	2.04	Base Case in the first set
Base Case, 7.2°	0.102	2.01	
Base Case, 5°	0.113	2.24	
Base Case, 1°	0.165	3.31	
Base Case, rollers	0.190	3.77	Roller boundary conditions
Case 2, 7.2°, 1st set	0.430	0.45	Case 2 in the first set
Case 2, 7.2°	0.486	0.40	
Case 2, 7.2°, fine	0.503	0.41	Fine mesh
Case 2, 7.2°, coarse	0.308	0.34	Coarse mesh
Case 2, 5°	0.605	0.49	
Case 2, 1°, coarse	0.689	0.65	Coarse mesh
Case 2, rollers	1.248	0.97	Roller boundary conditions

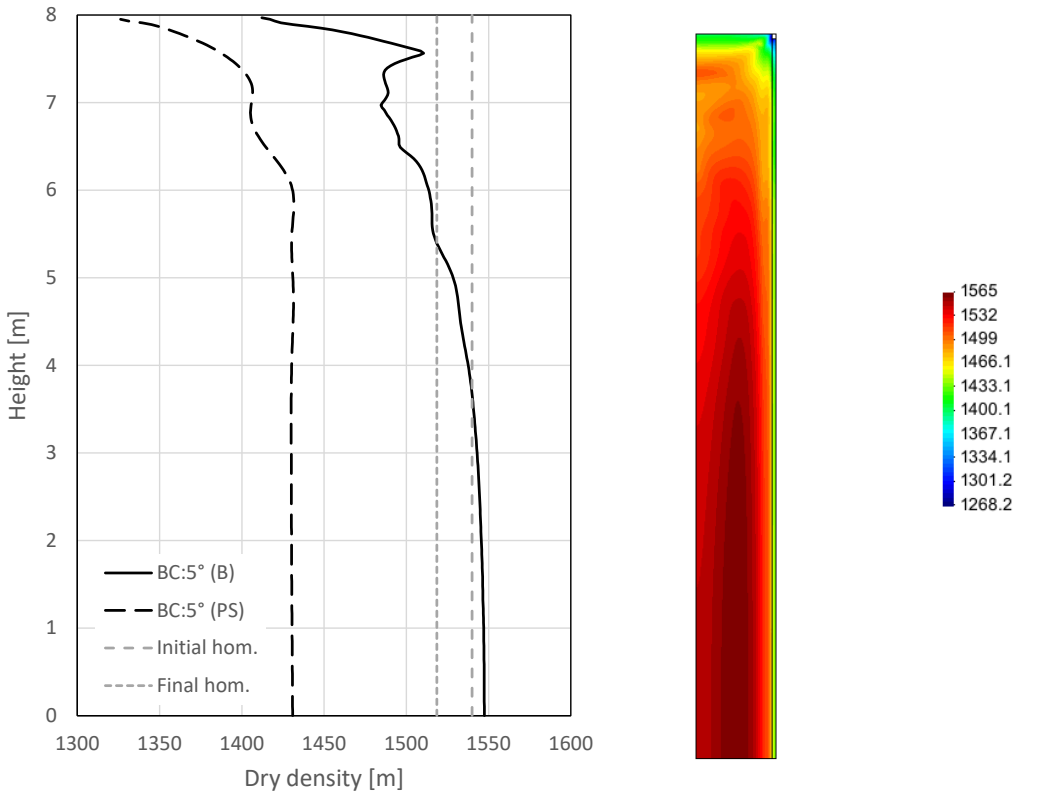

Figure 5-2. Base Case, 5°: Vertical profiles of the dry density field along the symmetry axis and rock wall boundary together with the averaged values in the initial and final configurations (left). Map over the dry density field at the final state (right).

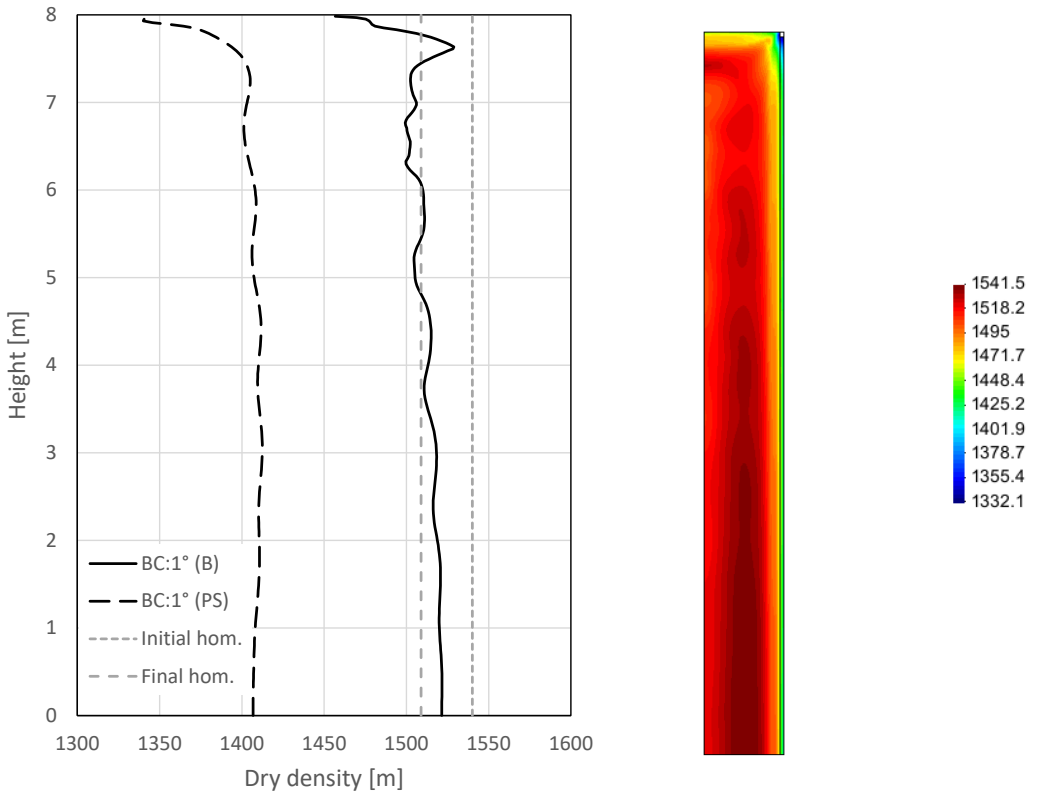

Figure 5-3. Base Case, 1°: Vertical profiles of the dry density field along the symmetry axis and rock wall boundary together with the averaged values in the initial and final configurations (left). Map over the dry density field at the final state (right).

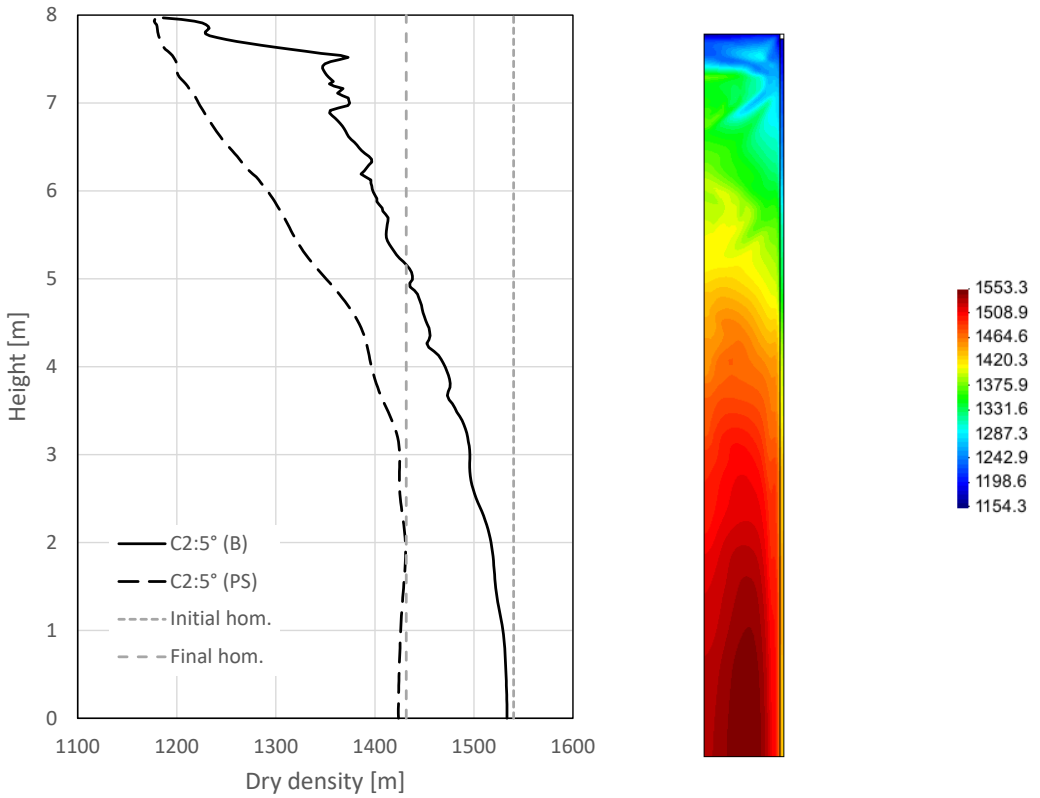

Figure 5-4. Case 2, 5°: Vertical profiles of the dry density field along the symmetry axis and rock wall boundary together with the averaged values in the initial and final configurations (left). Map over the dry density field at the final state (right).

6 Discussion and analysis

In this chapter the results are studied and discussed in greater detail. Proper solutions have been obtained for all cases except C2:1° in the second set, which was known to be challenging beforehand. Results from a proper solution for C2:1° may, however, be interpolated using results from C2:5° and C2:rollers.

For clarity it is here again repeated that the present study focus on how the buffer in an isotherm idealized KBS-3V setup behaves mechanically for the extreme case where the TB remains dry during water uptake of the deposition hole buffer.

This chapter starts below with identifying some issues which could give unrepresentative solutions. In section 6.1 the difference when the BC-model is evaluated using a pressure and dry density criterion is studied. Thereafter follow an analysis and discussion of the first set and second set of simulations, in section 6.2 and section 6.3, respectively.

Below follows a list of issues which could lead to misalignment with the problem formulation as given in the provided documentation:

- The utilized SR-Site swelling pressure curve does not agree with the one given in the problem formulation documentation. As discussed in 3.1, the magnitude of this disagreement was understood after the modelling was finished.
- Assuming a perfect bond between the tunnel backfill material and the buffer materials will introduce a stiffening of the system. It could be argued that in a real repository, friction (some bond) should be present between different components. At the “corner” where B, PS and TB meet, perfect adhesion is, however, likely to give overly restricted conditions and generate stress/strain concentrations which may affect the mechanical response of the system. Much effort has been spent trying to decrease the stiffening and the analysis of the BC-model in 4.1 indicates that it has been somewhat successful.
- When the elements, used in the solution scheme, are deformed significantly, the numerical solution becomes less accurate. At the top of the buffer the elements undergo large deformation.
- A large strain formulation has not been used. It could be noted that what often is called updated Lagrangean formulation in the Code_Bright framework is only using updated coordinates. A proper updated Lagrangean formulation would require an objective stress update scheme which presently is not included in Code_Bright. Using the updated coordinate option, however, resolves issues with updating the porosity field.
- Using a linear elastic material model together with the updated coordinates formulation results in an incrementally linear mechanical model. It is not straightforward when using this for representing the specified linear elastic TB reaction. The TB representation is also calibrated assuming uniaxial conditions. The representation of the TB is, however, not considered a big issue, it is more of an inconvenience.

6.1 Pressure criterion vs. dry density criterion

The friction forces at the hole wall will act as to restrain the upward swelling and thereby act together with the TB to keep the buffer in the deposition hole and aid pressure build-up in the buffer. This is of importance since microbial activity, and thereby sulphide driven copper corrosion, has been connected to pressure in the clay, see Posiva SKB (2017). When the pressure in the clay is above some value the microbial activity is drastically reduced. Thus, to suppress microbial activity the pressure should be larger than some lower limit for all points within the buffer. This criterion in terms of pressure is often translated into a criterion in terms of dry density using a swelling pressure curve.

With the above in mind, the solution of the BC model is evaluated using a pressure criterion and a corresponding dry density criterion. The results from the two evaluations are then compared. This will give an indication of what is lost in translation when going from the pressure criterion to dry density criterion using the pressure swelling curve.

To do this analysis, a criterion for the pressure, a lower pressure where microbes are inactivated, was taken from Posiva SKB (2017), suggesting 2 MPa. It should here be pointed out that 2 MPa might not be the criterion finally used by SKB. The magnitude is however likely to be relevant. For the transformation of this pressure criterion to dry density, the swelling pressure curve given in Table 2-9 was utilized. 2 MPa corresponds to a dry density of 1415 kg/m^3. It can be noticed that none of the simulated cases fully meets the criteria.

The left iso-map in Figure 6-1 shows dry densities above 1415 kg/m^3 in the upper 1.4 m of the buffer for the BC simulation. The dry density criterion is violated at the upper corner of the B material and also in a significant upper part, about 1.3 m, of the PS filling. The pressure field, in the same part of the geometry, can be evaluated in the right iso-map in Figure 6-1 where effective pressures above 2 MPa are shown. The pressure criterion is here only violated at the upper corner of the B and pellet filled slot.

The reason for the difference when using the two criteria is that the PS material has been compacted by the B material which, for a given dry density, results in pressures exceeding those given by the swelling pressure curve. This can be seen in Figure 4-1 where what is called the 'low swelling pressure curve' is generated by the expression in Table 2-9. This behaviour including hysteresis is considered a true mechanism of bentonite, not only a quirk of the model. At full saturation, however, pressures below the swelling pressure curve are not expected. It should here be pointed out that the swelling pressure curve itself can be lowered, for instance when the water composition is changed. The swelling pressure may then change without changing dry density. If the swelling pressure curve can be considered unaltered throughout the simulation, however, the criterion expressed in terms of dry density is equal to or is more conservative as compared to the criterion expressed in terms of pressure.

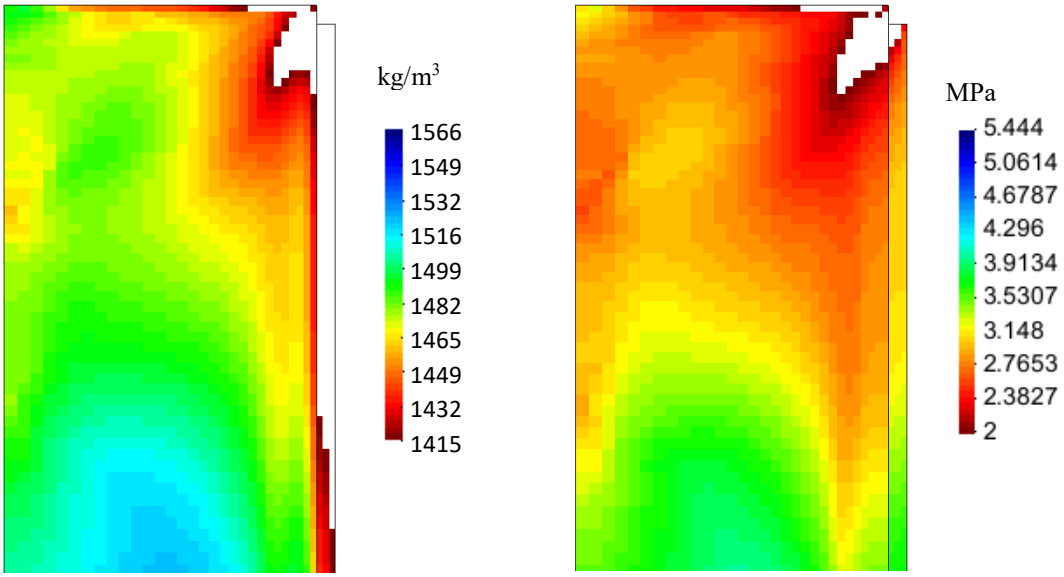

Figure 6-1. Base Case simulation iso-maps over the top 1.4 m of the buffer. Dry density with cut off at 1415 kg/m^3 (left). Effective pressure with cut off at 2 MPa (right).

6.2 First set of cases

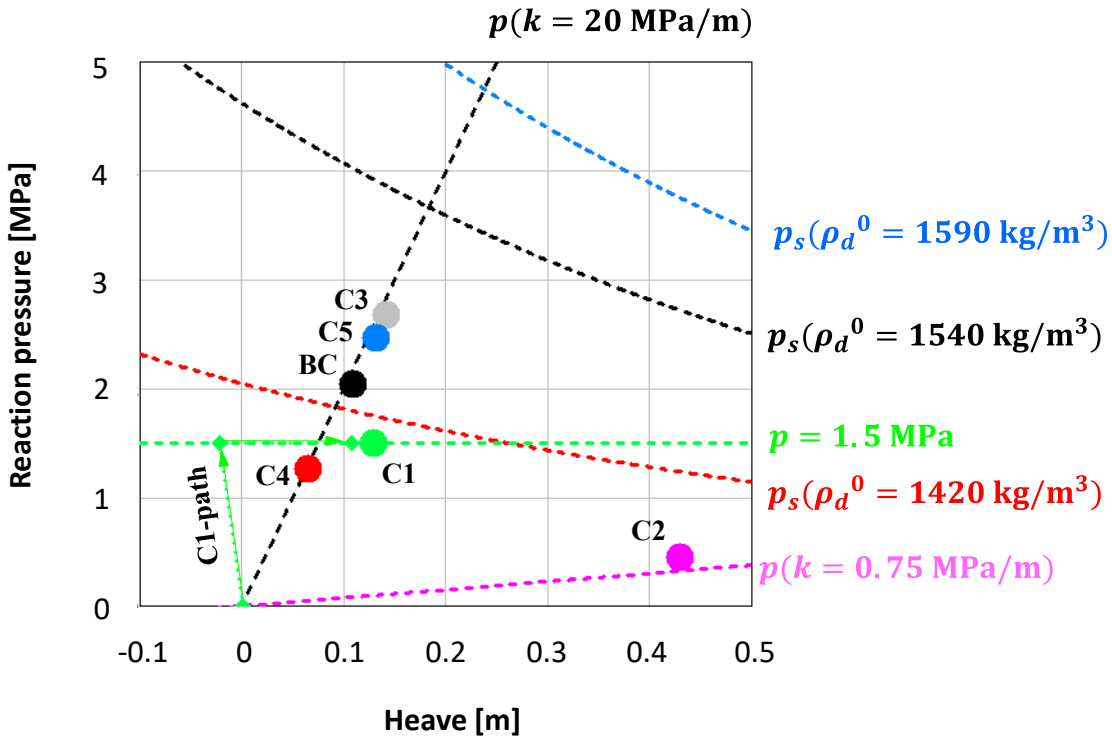

Figure 6-2. Compilation of FE-results and analytical expressions for the first set of cases.

For the first set of cases, {BC, C1 … C5} the global response/states at equilibrium, in terms of heave and average reaction pressure over the buffer top surface, are indicated by filled circles which can be identified by their "ID" in Figure 6-2. Idealised TB representations are indicated by following lines: long dashed black (k = 20 MPa/m), dashed pink (k = 0.75 MPa/m), dashed green (p = 1.5 MPa). Swelling pressure lines (using the relation in Table 2-9) starting from 1420 kg/m^3 (dashed red), 1540 kg/m^3 (dashed black), and 1590 kg/m^3 (dashed blue), are also given. In general, the solutions fit the corresponding idealised TB quite well.

The difference in response when using different idealised TB is clearly visible when studying the obtained equilibrium states of BC, C1 and C2 in Figure 6-2. BC and C2 have the same type of response where the state follows the specified loading curves. As for C1, to arrive at the specified 1.5 MPa vertical load on its top surface, the buffer was first compressed without allowing water to enter when gradually applying the load (green arrow upwards left). During compression the minimum elastic bulk modulus was increased to 200 MPa to avoid large compressive strains. At 1.5 MPa vertical load water was allowed to enter, and the buffer swelled (green arrow to the right). The green circular symbol indicates the state for C1 when adopting the compressed state as the reference.

Studying the dry density profiles for the three cases, repeated in Figure 6-3, BC and C2 is more similar in character as compared to C1. The C2 profile is just that of the BC but gone further, which is also seen when comparing dry density iso-maps shown to the right in Figure 6-3. C1, however, is somewhat different in that its dry density at the bottom is higher as compared to BC and C2. The buffer in C1 also shows less radial homogenisation. This probably comes from the difference in loading history.

It is suggested that the C1 simulation should be considered with some caution. The loading history used to achieve the specified 1.5 MPa might introduce effects on the mechanics of the system in such a way as not to obtain the case intended.

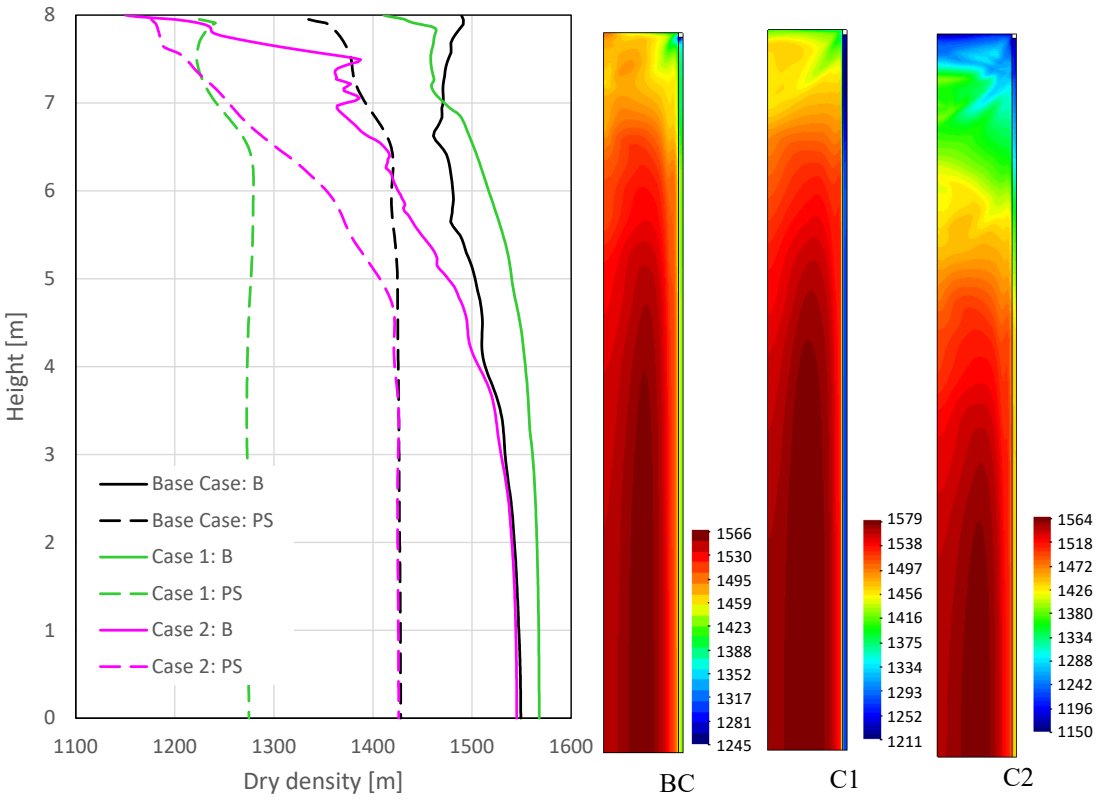

Figure 6-3. Dry density profiles of BC, C1, and C2 with the homogenised dry density in the initial state, 1540 kg/m³, indicated (left). Dry density fields for BC, C1, and C2 (right). Note that the colour scales do not match between the cases.

Comparing the BC and C3 in Figure 6-2 gives an indication of how different wetting affect the global state of the system. When wetting takes place from the bottom (as in C3) the restraining reaction from the wall friction has less influence which shows in increased heave and reaction pressure. The heave in C3 is 30 % higher as compared to the BC simulation.

If comparing the dry density profiles and iso-maps, given in Figure 6-4, the large difference between the cases is obvious. The buffer in C3 has swollen significantly at the bottom but not as much as in the BC at the top. In C3 the buffer has also homogenised to a higher degree in the radial direction.

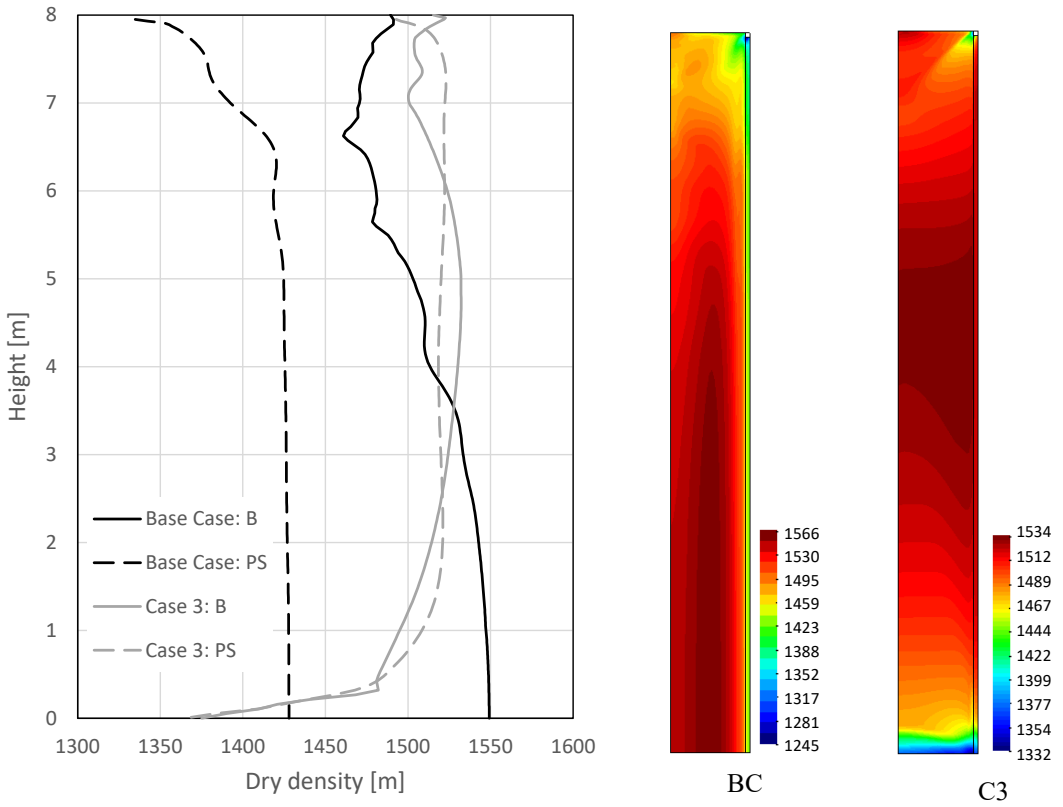

Figure 6-4. Dry density profiles and iso-maps of BC and C3. The homogenised dry density in the initial state, 1540 kg/m³, is indicated in the graph. Note that the colour scales do not match between the cases.

If focusing on how different initial dry densities affect the heave/reaction pressure, BC, C4 and C5 can be compared. Dry density is here defined as the homogenised value of the B and PS components. The left graph in Figure 6-5 shows the obtained heave against initial dry density, and as expected, C5 ($\rho_d{}^0 = 1590\ \mathrm{kg/m^3}$) gives more heave than BC ($\rho_d{}^0 = 1540\ \mathrm{kg/m^3}$), which in turn gives more heave than C4 ($\rho_d{}^0 = 1420\ \mathrm{kg/m^3}$).

The magnitude of heave can also be related to what could be expected for friction-free conditions. This shows to what extent the wall friction restrains the heave for different initial dry densities. The heave at friction-free conditions is here estimated as the states obtained at the intersection between the line $p(k = 20\ \mathrm{MPa/m})$ and the functions $p_s(\rho_d{}^0 = 1540\ \mathrm{kg/m^3})$, $p_s(\rho_d{}^0 = 1420\ \mathrm{kg/m^3})$, and $p_s(\rho_d{}^0 = 1590\ \mathrm{kg/m^3})$, respectively. The mid graph in Figure 6-5 shows the ratio between heave obtained from the numerical solution and the corresponding heave obtained from the analytical solution plotted against the dry density. The trend of the data shows that the higher the initial dry density the less the relative heave. Thus, the higher the initial dry density the more "efficient" the wall friction restrains the heave.

To get an overview of the final state in terms of dry density, the right graph in Figure 6-5 gives the obtained final homogenised dry densities for the three initial dry densities.

The dry density profiles and iso-maps, given in Figure 6-6, show no big surprises. The shape of the BC profiles is different compared to the other two.

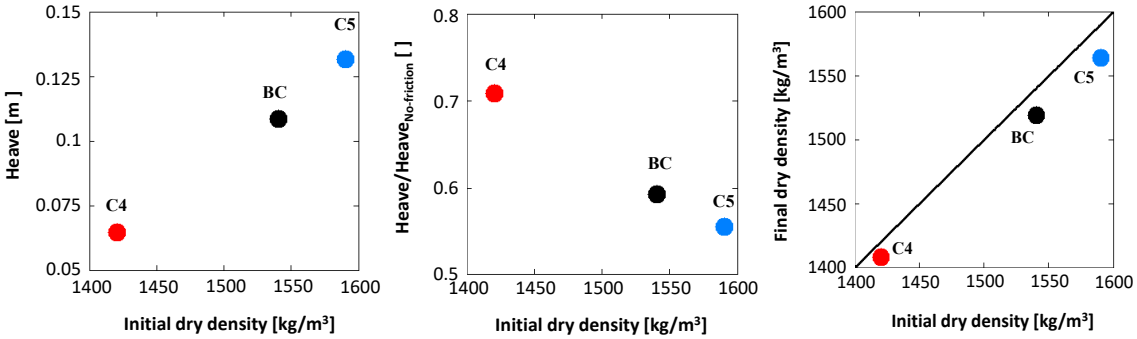

Figure 6-5. Buffer heave and final dry density dependency on initial dry density.

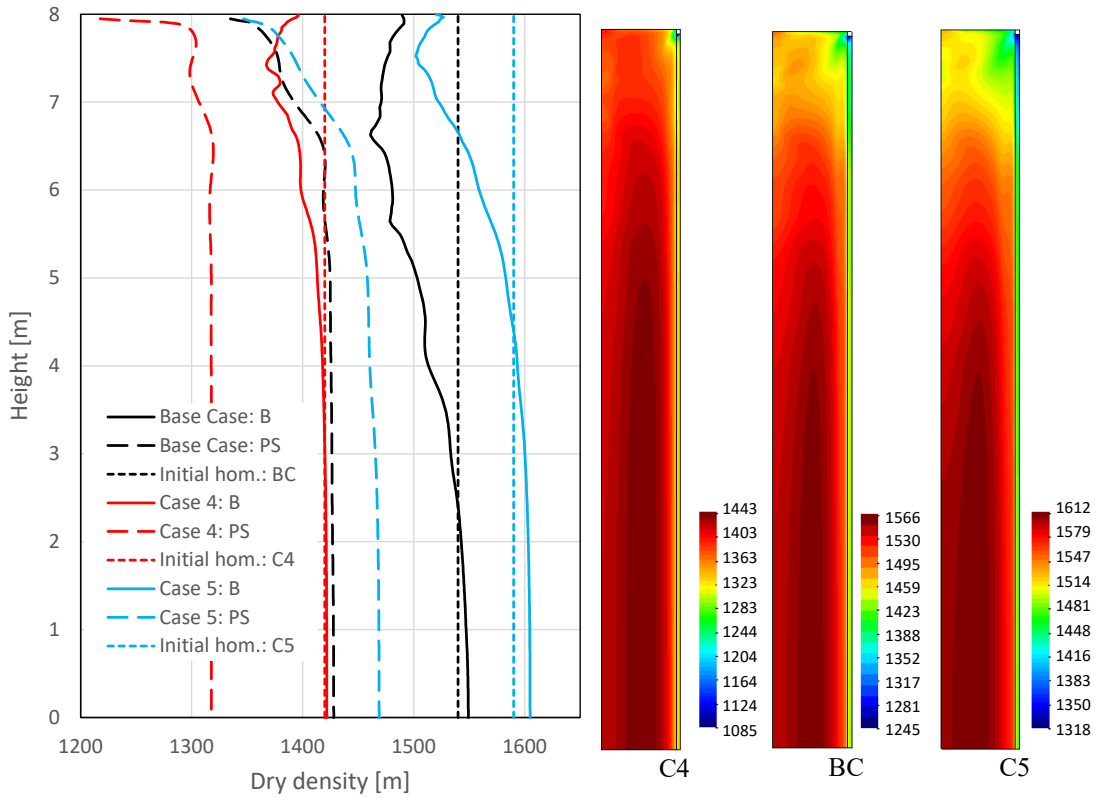

Figure 6-6. Dry density profiles and iso-maps of C4, BC, and C5. The homogenised dry densities at the initial states, 1420, 1540, and 1590 kg/m³, are indicated in the graph. Note that the colour scales do not match between the cases.

6.3 Second set of cases

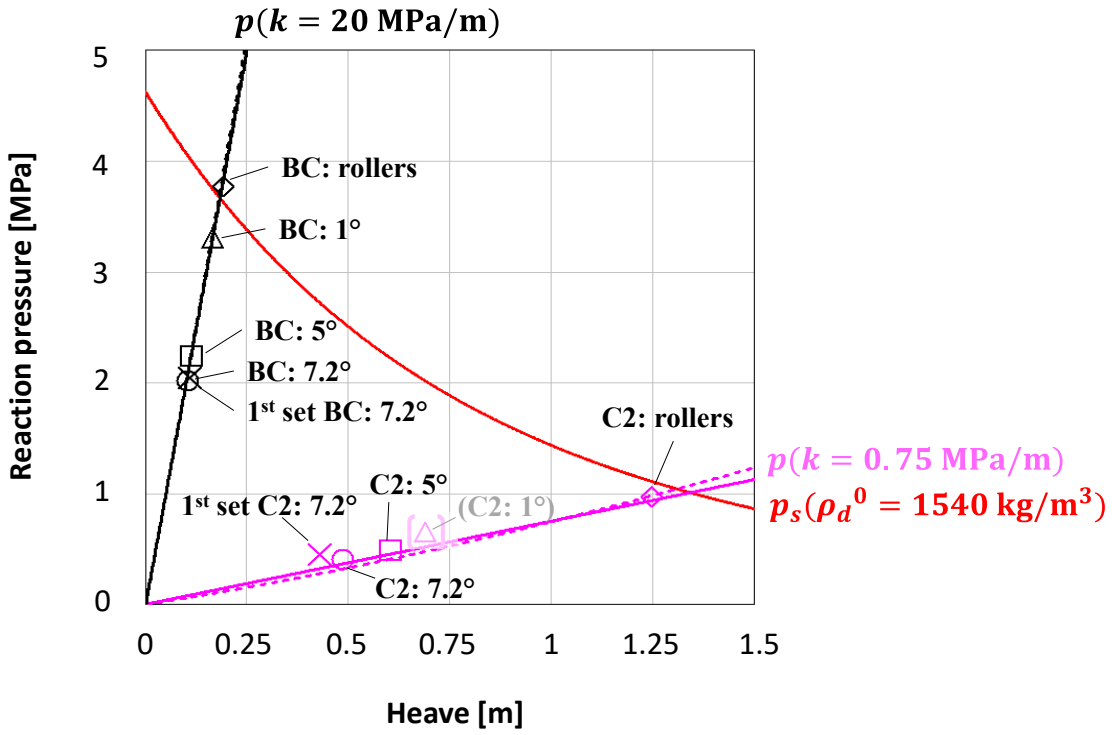

Figure 6-7. Compilation of FE-results and analytical expressions relevant for the second set of cases.

The global results for the second set, {BC:7.2°, BC:5°, BC:1°, BC:rollers, C2:7.2°, C2:5°, C2:1°, C2:rollers}, again expressed in terms of heave and reaction pressure, are shown in Figure 6-7. The BC and C2 results from the first set simulations, where the friction angle was 7.2 °, are also included for reference. The specified TB representations, where k = 20 MPa/m or k = 0.75 MPa/m, are indicated by the black solid and pink solid line, respectively. A swelling pressure line, using the relation in Table 2-9, when starting from 1540 kg/m^3 (red solid line) is also given. Homogenised responses of TB representations used in the second set simulations are indicated by hatched lines. The agreement between hatched and solid lines indicates that the mechanical setups, consisting of TB materials and a spring boundary condition, are appropriate.

When studying the first and second set results for the case where the friction angle was 7.2°, {BC, BC:7.2°, C2, C2:7.2°}, and comparing the agreement of these to the idealised TB representations, the improvement in representation of the TB in the second set FE simulations is clear, especially so for the C2 models.

If studying how well the FE solutions of all BC and all C2 variants agree with the corresponding TB representation, the BC results generally agrees better as compared to the C2 results. This is what could be expected, given that C2 generally involves larger deformation which makes the FE solution less accurate. For 'C2:1°' the agreement with the TB representation is quite poor. The main reason is that, to get convergency, a significantly coarser mesh had to be used, and the solution therefore is too stiff and less accurate.

Turning to how different friction angles affect the heave/reaction pressure, in the left graph in Figure 6-8 heave is plotted against the used friction angle. The C2:1° result is included for completeness but has been bracketed since it should not be considered reliable due to its poor resolution. Trends for the BC and C2 results are clearly seen, the higher the friction angle the lower the heave.

In the middle graph in Figure 6-8 the heave was normalised using the heave from the solution using rollers. Again, the general trend is obvious, the higher the friction angle the lower the normalized heave. The normalised heave data also shows that the "relative efficiency" to restrain the buffer is somewhat greater for the lower TB stiffness.

To get an overview of the final state in terms of dry density, the right graph in Figure 6-8 gives the obtained final homogenised dry densities for the different friction angles.

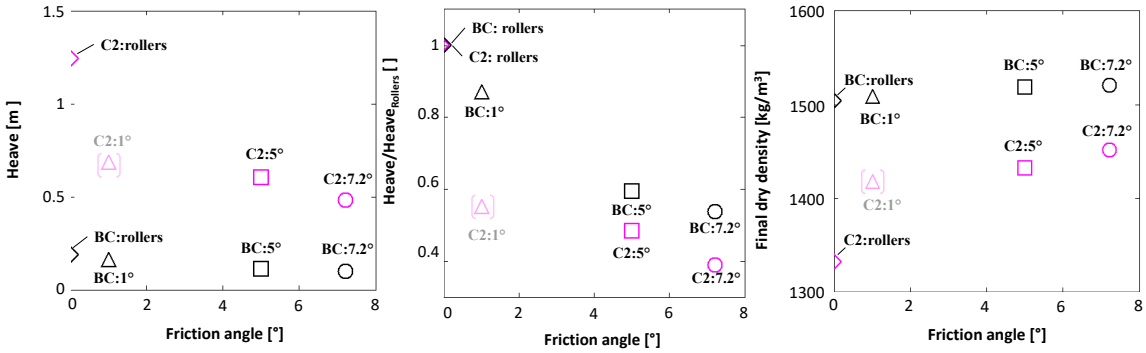

Figure 6-8. Buffer heave and final dry density dependency on friction angle.

Dry density profiles and iso-maps, relevant for the BC and C2 cases, are collected in Figure 6-9 and Figure 6-10, respectively. Both sets of results show clear overall behaviours that can be comprehended. At the saturated state, there is a remaining radial heterogeneity, i.e., the B and PS profiles differ. There is also an overall axial heterogeneity where the dry density profiles decrease at the top of the buffer. Lower friction angle in general results in more homogeneous profiles on a larger scale.

For the BC models, the radial heterogeneity's dependence on friction angle seems not to be very significant. For C2, the simulation using roller conditions shows significantly more radial heterogeneity as compared to the other simulations. The overall axial heterogeneity is also lower for that case.

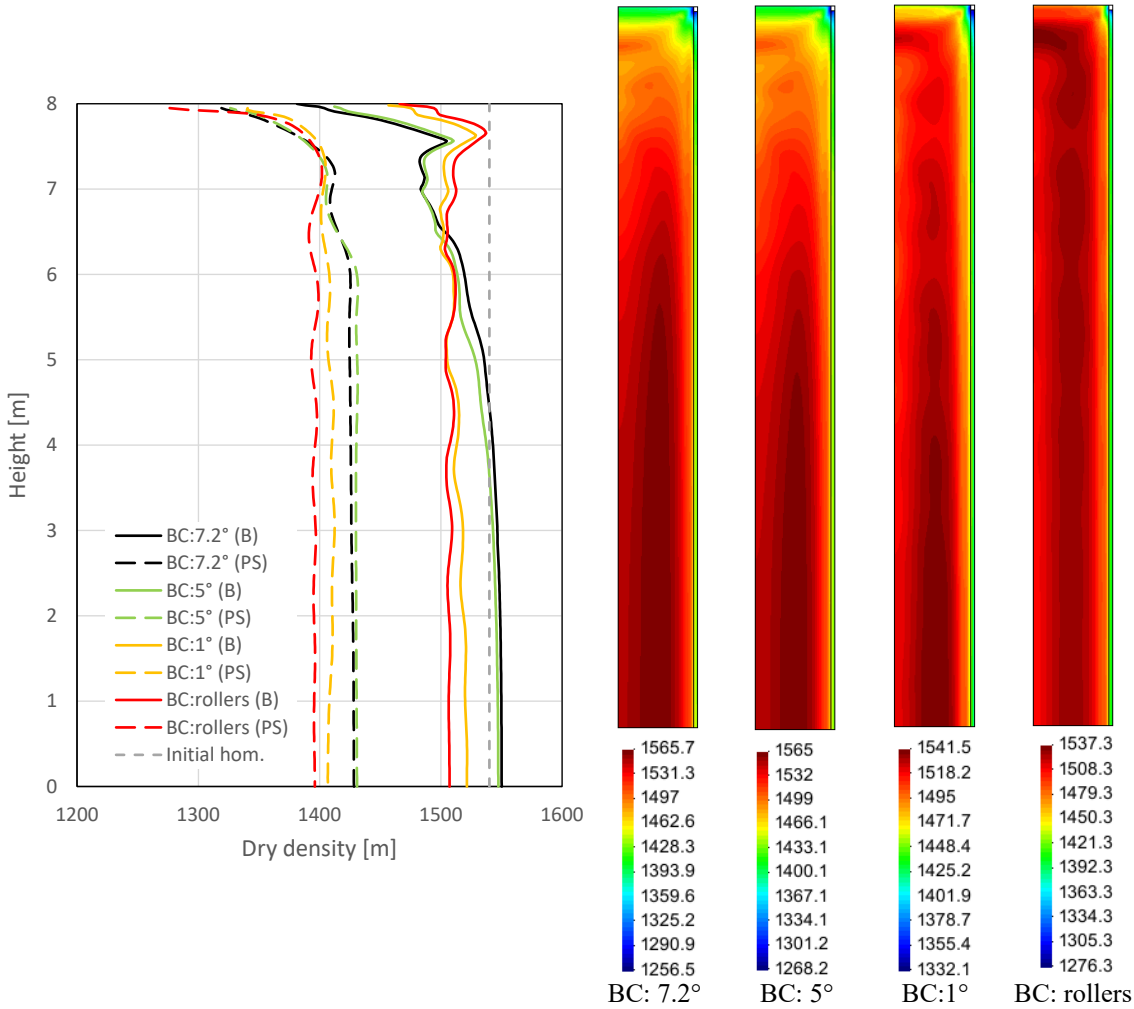

Figure 6-9. Dry density profiles and iso-maps of BC:7.2°, BC:5°, BC:1°, and BC:rollers. The homogenised dry density at the initial state, 1540 kg/m^3, is indicated in the graph. Note that the colour scales do not match between the cases.

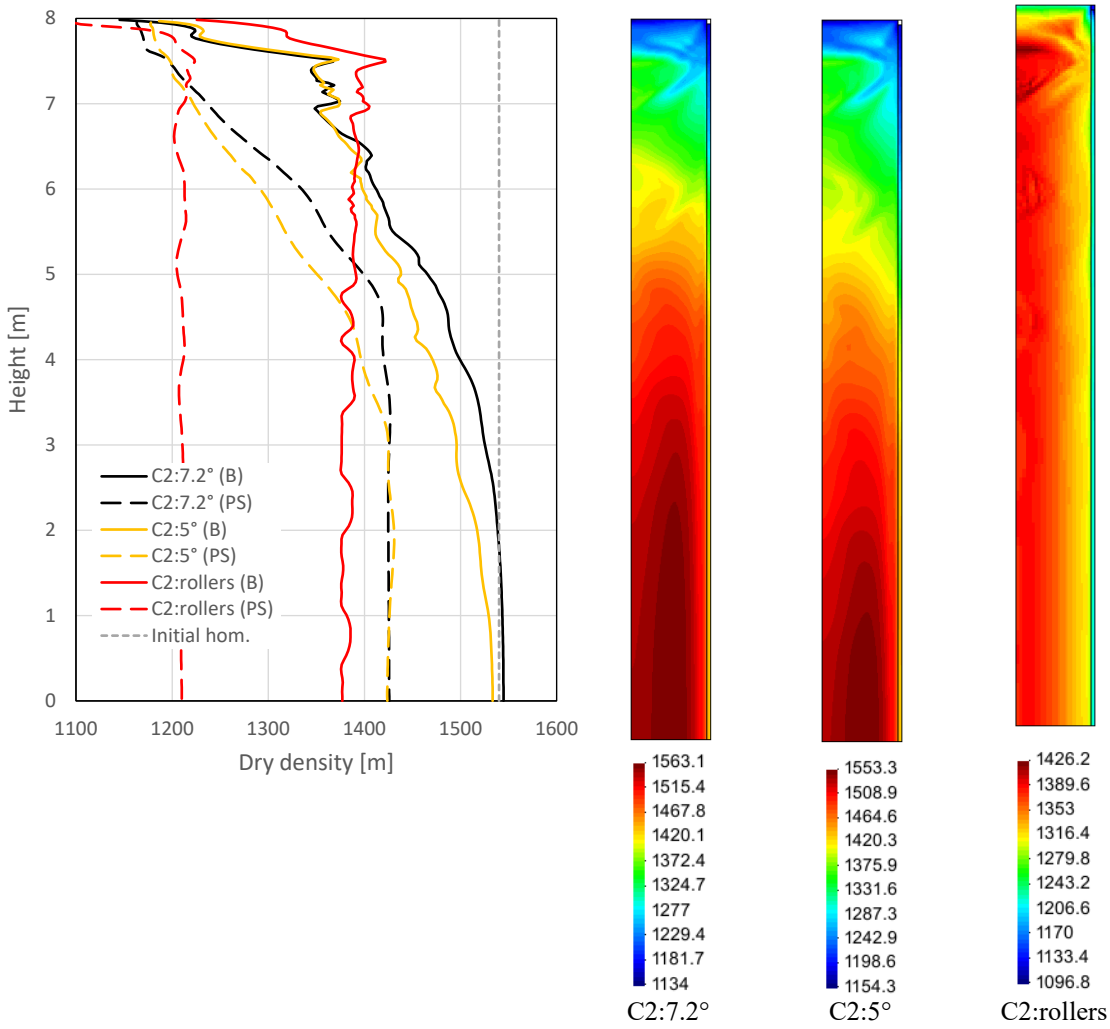

Figure 6-10. Dry density profiles and iso-maps of C2:7.2°, C2:5°, and C2:rollers. The homogenised dry density at the initial state, 1540 kg/m^3, is indicated in the graph. Note that the colour scales do not match between the cases.

7 Conclusions

Below follows conclusions from the numerical studies of how the buffer of an idealized KBS-3V design behaves mechanically for the extreme case where the tunnel backfill remains dry during water uptake of the deposition hole buffer.

General conclusions from the work are:

- The base case model shows proper mechanical behaviour. The mechanics of the buffer, the influence from the stress concentration at the interface between buffer and tunnel backfill, and the evaluated effective friction angle are all reasonable, see section 4.1.
- The simulations do in general fit the corresponding idealized tunnel backfill well. This indicates that the tunnel backfill is represented accurately, and that the models perform as expected. Exceptions were found when the discretization was too coarse, see section 5.1 and simulation C2:1° in section 6.3.
- Evaluation of the base case model when using a criterion expressed in terms of dry density is equally or more conservative as compared to when a criterion expressed in terms of pressure is used. The dry density criterion was obtained from using a pressure criterion together with the adopted swelling pressure curve.

Conclusions from the 1st set of models:

- When wetting takes place from the bottom:
    - The restraining reaction from the wall friction has less influence which shows in increased heave and reaction pressure.
    - The buffer swells significantly at the bottom but not so much at the top.
    - The buffer homogenizes to a higher degree in the radial direction.
- The higher the initial dry density the higher the heave of the top buffer surface.
- The higher the initial dry density the less the relative heave (= heave normalized against a model without wall friction). Thus, the higher the initial dry density the more “efficient” the wall friction restrains the heave.

Conclusions from the 2nd set of models:

- The higher the friction angle the lower the heave and the relative heave (= heave normalized against a model without wall friction).
- The relative heave data also shows that the “relative efficiency” to restrain the buffer is somewhat greater for the lower tunnel backfill stiffness.
- Dry density fields findings:
    - They exhibit a remaining radial and vertical heterogeneity.
    - Lower friction angle in general results in more homogeneous profiles on a larger scale.
    - For the base case, the radial heterogeneity’s dependence on friction angle seems not to be very significant.
    - For the lower tunnel backfill stiffness, the simulation without wall friction shows significantly more radial heterogeneity as compared to the other simulations. The overall axial heterogeneity is also lower in the model without friction.

References

SKB's (Svensk Kärnbränslehantering AB) publications can be found at www.skb.com/publications.

Alcoverro J, Alonso E, 2001. Scientific bases of Code_Bright. 70-UPC-L-1-001: 1-12, UPC, Spain.

Dueck A, 2004. Hydro-mechanical properties of a water unsaturated sodium bentonite: Laboratory study and theoretical interpretation. PhD thesis. Lund University, Sweden.

Dueck A, Börgesson L, Kristensson O, Malmberg D, Åkesson M, Hernelind J, 2019. Bentonite homogenisation. Laboratory study, model development and modelling of homogenisation processes. SKB TR-19-11, Svensk Kärnbränslehantering AB.

Glamheden R, Fälth B, Jacobsson L, Harrström J, Berglund J, Bergkvist L, 2010. Counterforce applied to prevent spalling. SKB TR-10-37, Svensk Kärnbränslehantering AB.

Posiva SKB, 2017. Safety functions, performance targets and technical design requirements for a KBS-3V repository. Conclusions and recommendations from a joint SKB and Posiva working group. Posiva SKB Report 01, Posiva Oy, Svensk Kärnbränslehantering AB.

Sandén T, Kristensson O, Lönnqvist M, Börgesson M, Nilsson L, Goudarzi R, 2020. Buffer swelling. Laboratory tests and modelling. SKB TR-20-04, Svensk Kärnbränslehantering AB.

Sellin P (ed), Åkesson M, Kristensson O, Malmberg D, Börgesson L, Birgersson M, Dueck A, Karnland O, Hernelind J, 2017. Long re-saturation phase of a final repository. Additional supplementary information. SKB TR-17-15, Svensk Kärnbränslehantering AB.

Svensson D, Lundgren C, Johannesson L-E, Norrfors K, 2017. Developing strategies for acquisition and control of bentonite for a high level radioactive waste repository. SKB TR-16-14, Svensk Kärnbränslehantering AB.

Åkesson M, Börgesson L, Kristensson O, 2010. SR-Site data report. THM modelling of buffer, backfill and other system components. SKB TR-10-44, Svensk Kärnbränslehantering AB.

Appendix A Theory

The following description of the hydro-mechanical theory, on which Code_Bright is based, is a brief and less general version of what is given in Alcoverro and Alonso (2001). Constant temperature (T = 20 °C) and gas pore pressure (p_g = 0.1 MPa) have been used in the current simulations and no air was allowed to be dissolved into the liquid phase. Wherever these two variables appear in the formulation they should be considered constant.

The theory used in Code_Bright has its roots in a traditional geomechanical porous formulation, based on considering the material as a mixture of the constituents:

minerals,

liquid water,

dissolved air,

water vapor, and

dry air.

The constituents are divided in three *components* (i): minerals (m), water (w), and air (a) (the component belonging of entities is indicated by a superscript) and an assumption of three *immiscible phases* (α): solid (s), liquid (l), and gas (g) (the phase belonging of entities is indicated by a subscript) are made. The solid phase only consists of the mineral component, so the component superscript index (m) will not be written in the following.

From considering the structural assumptions of the mixture, following primitives may be defined:

mixture volume element (v),

solid phase volume (v_s),

liquid phase volume (v_l),

gas phase volume ($v_g = v - v_s - v_l$), and

pore volume ($v_p = v - v_s$).

Further primitives, regarding mass and energy are introduced for the constituents:

solid mass (m_s),

water mass in liquid (m_l^w),

water mass in gas (i.e. water vapor mass) (m_g^w),

dry air mass in gas (m_g^a).

With use of the primitives above the definitions below may be formulated:

porosity ($\phi = v_p/v$),

solid density ($\rho_s = m_s/v_s$),

liquid water mass per liquid phase volume ($\theta_l^w = m_l^w/v_l$),

water vapor mass per gas phase volume ($\theta_g^w = m_g^w/v_g$),

dry air mass per gas phase volume ($\theta_g^a = m_g^a/v_g$),

degree of liquid saturation ($S_l = v_l/v_p$), and

degree of gas saturation ($S_g = v_g/v_p$).

Below, e.g. when describing commonly used constitutive laws, functions that give values of variables are indicated with ~ above the variable name.

Balance relations

The solid mass per mixture volume element can be expressed,

$$\frac{m_s}{v} = \frac{m_s}{v_s}\frac{v - v_p}{v} = \rho_s(1-\phi). \tag{A-1}$$

and by using this as a basis, the balance equation,

$$\frac{\partial}{\partial t}\big(\rho_s(1-\phi)\big) + \nabla\cdot\rho_s(1-\phi)\frac{d\boldsymbol{u}}{dt} = 0\,, \tag{A-2}$$

can be derived. If the above is integrated, an updating scheme for the porosity is obtained,

$$J_s\rho_s(1-\phi) = {\rho_s}^0(1-\phi^0)\,, \tag{A-3}$$

where J_s is the determinant of the of the deformation gradient of the solid skeleton, $J_s = \det\left(\frac{\partial \boldsymbol{u}}{\partial \boldsymbol{X}}\right) + 1$, and the superscript ^{0} denotes initial values of variables.

The water mass per mixture volume element can be expressed as,

$$\frac{m^w}{v} = \frac{m_l^w + m_g^w}{v} = \theta_l^w S_l\phi + \theta_g^w S_g\phi. \tag{A-4}$$

If introducing a source term f^w and fluxes of water in the liquid and gas phase, $\boldsymbol{j}_l^w$ and $\boldsymbol{j}_g^w$, the continuity equation,

$$\frac{\partial}{\partial t}\left(\theta_l^w S_l\phi + \theta_g^w S_g\phi\right) + \nabla\cdot\left(\boldsymbol{j}_l^w + \boldsymbol{j}_g^w\right) = f^w\,, \tag{A-5}$$

can be derived.

The used quasi-static formulation of the balance of momentum for the porous media reads,

$$\nabla\cdot\boldsymbol{\sigma} + \boldsymbol{b} = \boldsymbol{0}\,, \tag{A-6}$$

in terms of total stress, $\boldsymbol{\sigma}$, and body force, $\boldsymbol{b}$. As can be seen (from the absent inertia term), a mechanical equilibrium condition assuming an insignificant effect from inertia (i.e. quasi-static conditions), has been used. In the present formulation ordinary continuum mechanics sign conventions are used, i.e. stress components are positive for tensile conditions.

In addition to the balance equations, two equilibrium restrictions have been used. The mechanical and phase change equilibrium restriction are described in the next section.

In order to close the formulation, variables are selected as independent or dependent and material specific constitutive relations are specified where dependent variables are given by expressions of independent variables. The independent variables in Code_Bright are p_l and $\boldsymbol{u}$. The liquid pore pressure and displacement vector. Initial and boundary conditions are finally selected as completely specify the problem formulation.

It should here be mentioned that the liquid pore pressure loses its ordinary physical meaning for a bentonite type of material where the chemical potential governs the processes. For such materials the pore pressure could be considered an entity describing the material's water absorption potential.

Equilibrium restrictions

For the present systems accelerations are assumed insignificant. This *mechanical equilibrium condition* makes its appearance in the used quasi-static form of the balance of momentum.

The *phase change equilibrium* may be taken as manifested through the equality between chemical potentials of a constituent in different phases. Assuming phase change equilibrium for water and that the gas phase is a mixture of two ideal gases (air and water vapor) give the phase change equilibrium for water,

$$\tilde{\theta}_g^w(p_l,T) = \frac{\tilde{p}_g^w(T)M_w}{R(273.15+T)}\exp\left(\frac{-\big(p_g - p_l\big)M_w}{R(273.15+T)\tilde{\rho}_l(p_l,T)}\right). \tag{A-7}$$

In the expression above, the physical parameters molar mass of water, M_w, and the constant of gases, R, appear.

Constitutive relations

As mentioned earlier, to close the formulation, variables are selected as independent or dependent and material specific constitutive relations are specified where dependent variables are given by expressions of independent variables; in Code_Bright liquid pore pressure and displacement. Thus, liquid pore pressure and displacement become the unknowns to be solved for.

Porous medium relations

These constitutive relations describe interactions between constituents in various phases.

The degree of liquid saturation of the porous medium is related to the liquid pore pressure by use of a *retention law*,

$$S_l = \widetilde{S_l}(p_l). \tag{A-8}$$

The degree of gas saturation is given by,

$$\tilde{S_g}(p_l) = 1 - \widetilde{S_l}(p_l). \tag{A-9}$$

The mass fluxes are additively decomposed in terms of a non-advective (diffusive), $\boldsymbol{i}_\alpha^i$, and an advective, $\theta_\alpha^i \boldsymbol{q}_\alpha$, contribution, according to,

$$\boldsymbol{j}_\alpha^i = \boldsymbol{i}_\alpha^i + \theta_\alpha^i \boldsymbol{q}_\alpha, \alpha = l, g \quad i = w, a \text{ without the combination } \alpha, i = l, a \tag{A-10}$$

The *advective* mass fluxes include the phase velocity, $\boldsymbol{q}_\alpha$, which for the liquid typically is given by Darcy's law, schematically given by,

$$\boldsymbol{q}_l = \widetilde{\boldsymbol{q}}_l(p_l). \tag{A-11}$$

and which for the gas phase becomes zero since the pressure is taken to be constant in the present work. Darcy's law is obtained from a combination of balance of momentum of the fluid phases together with constitutive assumptions of momentum exchange with other phases.

Diffusive (or non-advective) mass fluxes are usually described by Fick's law, schematically given by:

$$\boldsymbol{i}_g^w = \tilde{\boldsymbol{i}}_g^w\left(\theta_g^w\right), \tag{A-12}$$

in the case of the water vapor. Fick's law is obtained by consideration of: the constituent balance of momentum, the phase balance of momentum and the exchange of momentum with the other constituents.

The remaining diffusive (non-advective) mass fluxes are specified by the relations:

$$\sum_{i=w,a} \boldsymbol{i}_\alpha^i = \boldsymbol{0}, \alpha = l, g \tag{A-13}$$

Solid phase relations

In Code_Bright the *solid phase density* is given by,

$$\rho_s = \tilde{\rho}_s(T) \tag{A-14}$$

The mechanical constitutive relation for the solid phase is not explicitly given in terms of the *solid phase stress*. Instead, the mechanical relation incorporating the solid phase is formulated in terms of *total stress*, $\boldsymbol{\sigma}$, of the porous medium and the constitutive relations of the stress tensors of the fluid phases (pressures, p_α).

A rate form of a schematic mechanical material model for unsaturated conditions can be expressed,

$$\begin{aligned} \frac{d}{dt}\left(\boldsymbol{\sigma} + p_g \boldsymbol{I}\right) &= \boldsymbol{D}\frac{d\boldsymbol{\varepsilon}}{dt} + \boldsymbol{h}\frac{d\left(p_g - p_l\right)}{dt} \\ \boldsymbol{D} = \widetilde{\boldsymbol{D}}\left(\boldsymbol{\sigma} + p_g \boldsymbol{I}, p_g - p_l\right), \boldsymbol{h} &= \widetilde{\boldsymbol{h}}\left(\boldsymbol{\sigma} + p_g \boldsymbol{I}, p_g - p_l\right), \end{aligned} \tag{A-15}$$

where the material time derivative is given by,

$$\frac{d}{dt}(\cdot) = \frac{\partial}{\partial t}(\cdot) + \frac{d\boldsymbol{u}}{dt} \cdot \nabla(\cdot). \tag{A-16}$$

The small strain tensor $\boldsymbol{\varepsilon}$ is given by the displacements according to,

$$\boldsymbol{\varepsilon} \equiv \frac{1}{2}\left(\frac{\partial \boldsymbol{u}}{\partial \boldsymbol{X}} + \left(\frac{\partial \boldsymbol{u}}{\partial \boldsymbol{X}}\right)^T\right) \tag{A-17}$$

The unsaturated formulation is given in terms of $\boldsymbol{\sigma}' = \boldsymbol{\sigma} + p_g \boldsymbol{I}$ and $p_g - p_l$, often denoted net stress and suction, respectively.

When saturated states are considered, i.e. $p_g - p_l \leq 0$, the schematic mechanical material model is given by,

$$\begin{aligned} \frac{d}{dt}(\boldsymbol{\sigma} + p_l \boldsymbol{I}) &= \boldsymbol{D}\frac{d\boldsymbol{\varepsilon}}{dt} \\ \boldsymbol{D} &= \widetilde{\boldsymbol{D}}(\boldsymbol{\sigma} + p_l \boldsymbol{I}), \end{aligned} \tag{A-18}$$

now in terms of $\boldsymbol{\sigma}'' = \boldsymbol{\sigma} + p_l \boldsymbol{I}$, often denoted effective stress tensor.

Liquid phase relations

The liquid phase is considered an ideal solution of air in liquid water. The *liquid phase density* and *liquid phase viscosity*, both considered mixture properties, are given by specified functions,

$$\rho_l = \tilde{\rho}_l(p_l, T) \tag{A-19}$$

and

$$\mu_l = \tilde{\mu}_l(T)\,, \tag{A-20}$$

respectively.

Gas phase relations

Regarding the gas it should be remembered that a constant gas pore pressure, p_g = 0.1 MPa, has been used in the present simulations. The gas phase is considered an ideal gas mixture, thus *Dalton's law* is adopted

$$p_g = p_g^a + p_g^w\,. \tag{A-21}$$

The *water gas pore pressure* is described by,

$$p_g^w = \tilde{p}_g^w(T), \tag{A-22}$$

and the *air gas pore pressure* p_g^a is related to the density variable θ_g^a making it possible to write

$$\theta_g^a = \tilde{\theta}'^a_g\big(T, p_g - p_g^w(T)\big) = \tilde{\theta}_g^a\big(T, p_g\big)\,, \tag{A-23}$$

using Dalton's law.

Appendix B Model identification

Case	Model directory name	Comment
BC 1D	BC_test_v03_A_corr.gid	1D calibration model
Base Case	BC_v8B_corr.gid	
Case 1	C1_v006.gid	
Case 2	C2_v001.gid	
Case 3	C3_v03_corr	
Case 4 1D	C4_test_v01_corr.gid	1D calibration model
Case 4	C4_v01_corr.gid	
Case 5 1D	C5_test_v01_corr_p0.gid	1D calibration model
Case 5	BC_v8B_corr_C5_P0BC.gid	
BC:7.2°	BC_72_v021.gid	Updated Base Case simulation
BC:5°	BC_5_v021.gid	
BC:1°	BC_1_v021.gid	
BC: rollers	BC_72_v02_rollers.gid	
C2:7.2°	C2_72_v02.gid	Updated Case 2 simulation
C2:7.2° fine	C2_72_v02_fine.gid	High mesh density
C2:7.2° coarse	C2_72_v02_coarse.gid	Low mesh density
C2:5°	C2_5_v02.gid	
C2:1°	C2_1_v02_coarse.gid	Low mesh density
C2: rollers	C2_72_v02_rollers.gid	